ssDNA catenation. The omission of either EVL or topoisomerase quenched the ssDNA-catenating reaction, indicating that both proteins are essential for this reaction. A deletion analysis revealed that the EVL C-terminal domain, which possesses the annealing activity, is responsible for the ssDNA catenation. We also found that EVL physically interacted with human TOPO IIIα in a human cell extract and *in vitro*. These new findings suggest that EVL may function with a type I topoisomerase, such as TOPO IIIα, by catalyzing ssDNA cutting and re-joining reactions in the conversion of DNA intermediates during homologous recombination.

MATERIALS AND METHODS

Protein preparation

Human EVL, EVL(1–221) and EVL(222–418) were prepared by the methods described earlier (2,7). In these methods, human EVL, EVL(1–221) and EVL(222–418) were expressed as His_6-tagged proteins, and the His_6 tag was removed by a thrombin treatment during the purification procedure. Human RPA was produced in *E. coli* cells and was prepared according to the published protocol (19).

The DNA fragment encoding human TOPO IIIα was isolated from a human cDNA pool (purchased from Clontech Laboratories, Mountain View, CA, USA) by the polymerase chain reaction. The TOPO IIIα DNA fragment was cloned in the *Nde*I site of the pET15b vector (Novagen, Darmstadt, Germany). In this construct, the His_6 tag sequence was fused to the N terminus of the protein. Human TOPO IIIα was produced in the *E. coli* BL21(DE3) codon plus-RP strain (Stratagene, La Jolla, CA, USA) and was purified by the following procedure. The cells producing His_6-tagged TOPO IIIα were resuspended in a 50 mM Tris–HCl buffer (pH 7.5), containing 1M NaCl, 5 mM 2-mercaptoethanol and 10% glycerol, and were disrupted by sonication. The cell debris was removed by centrifugation for 20 min at 30 000*g*, and the lysate was mixed gently by the batch method with Ni-NTA agarose beads (3 ml, Qiagen, Hilden, Germany) at 4°C for 1 h. The His_6-tagged TOPO IIIα-bound beads were washed with 40 ml of 20 mM potassium phosphate buffer (pH 7.4), containing 500 mM NaCl, 5 mM 2-mercaptoethanol, 40 mM imidazole and 10% glycerol, and then were washed again with 40 ml of 20 mM potassium phosphate buffer (pH 7.4), containing 500 mM NaCl, 5 mM 2-mercaptoethanol, 30 mM imidazole and 10% glycerol. The beads were then packed into an Econo-column (Bio-Rad Laboratories, Hercules, CA, USA) and were washed with 90 ml of 20 mM potassium phosphate buffer (pH 7.4), containing 500 mM NaCl, 5 mM 2-mercaptoethanol, 30 mM imidazole and 10% glycerol. His_6-tagged TOPO IIIα was eluted with a linear gradient of 30–300 mM imidazole (13-column volumes), in 20 mM potassium phosphate (pH 7.4), 100 mM NaCl, 5 mM 2-mercaptoethanol and 10% glycerol. Peak fractions containing His_6-tagged TOPO IIIα were diluted 5-fold with a 20 mM potassium phosphate buffer (pH 7.4), containing 5 mM 2-mercaptoethanol and 10% glycerol and were mixed gently by the batch method with Hydroxyapatite resin (5 ml, Bio-Rad Laboratories) at 4°C for 1 h. The unbound fraction was then dialyzed against a 20 mM potassium phosphate buffer (pH 7.4), containing 100 mM NaCl, 5 mM 2-mercaptoethanol and 10% glycerol. After the dialysis, the sample was loaded on an SP Sepharose column (1 ml, GE Healthcare Biosciences, Uppsala, Sweden), which was equilibrated with 20 ml of 20 mM potassium phosphate buffer (pH 7.4), containing 100 mM NaCl, 5 mM 2-mercaptoethanol and 10% glycerol. The resin was washed with 20 ml of 20 mM potassium phosphate buffer (pH 7.4), containing 225 mM NaCl, 5 mM 2-mercaptoethanol and 10% glycerol, and the His_6-tagged TOPO IIIα was then eluted with a linear gradient of 225–600 mM NaCl (24-column volumes). The purified His_6-tagged TOPO IIIα was dialyzed against 20 mM HEPES–NaOH buffer (pH 7.5), containing 100 mM NaCl, 5 mM 2-mercaptoethanol and 20% glycerol, and was stored at −80°C. The concentration of the purified His_6-tagged TOPO IIIα was determined by the Bradford method (20), using bovine serum albumin as the standard.

Assays for DNA binding

The ϕX174 circular ssDNA (20 μM) was mixed with EVL in 10 μl of a standard reaction solution, containing 36 mM HEPES–NaOH (pH 7.5), 1 mM dithiothreitol, 4 mM 2-mercaptoethanol, 80 mM NaCl, 1 mM $MgCl_2$, 24% glycerol and 0.1 mg/ml bovine serum albumin. The reaction mixtures were incubated at 37°C for 15 min, and were then analyzed by 0.8% agarose gel electrophoresis in 1× TAE buffer (40 mM Tris–acetate and 1mM EDTA) at 3.3 V/cm for 2 h. The bands were visualized by ethidium bromide staining.

ssDNA-catenating assay

The ϕX174 circular ssDNA (20 μM) was incubated with EVL and Topo I (New England Biolabs, Ipswich, MA, USA), in a reaction buffer containing 24 mM HEPES–NaOH (pH 7.5), 1 mM $MgCl_2$, 1 mM Tris–HCl (pH 7.5), 1.1 mM dithiothreitol, 1 mM 2-mercaptoethanol, 20 mM NaCl, 5 mM KCl, 3.5 mM ammonium sulfate, 0.01 mM EDTA, 11% glycerol and 0.1 mg/ml bovine serum albumin, at 37°C for 1 h. For the experiments with TOPO IIIα, the reactions were conducted in a buffer containing 30 mM HEPES–NaOH (pH 7.5), 1 mM $MgCl_2$, 1 mM dithiothreitol, 2.5 mM 2-mercaptoethanol, 70 mM NaCl, 14% glycerol and 0.1 mg/ml bovine serum albumin. The samples were then deproteinized by a treatment with 0.2% SDS and 1.3 mg/ml proteinase K at 37°C for 15 min. The products were then incubated at 100°C for 5 min and were chilled on ice for 5 min. The products were separated by 1% agarose gel electrophoresis, and the bands were visualized by SYBR Gold (Invitrogen, Carlsbad, CA, USA) staining.

ssDNA-annealing assay

The ssDNA-annealing assay was performed as described earlier (2). Briefly, the ssDNA oligonucleotide 49-mer (0.2 μM) was incubated with the indicated amounts of

EVL or the EVL fragments at 30°C for 5 min, in 9 µl of reaction buffer, containing 28 mM HEPES–NaOH (pH 7.5), 50 mM NaCl, 2 mM 2-mercaptoethanol, 12% glycerol, 0.1 mM $MgCl_2$, 1 mM DTT and 0.1 mg/ml bovine serum albumin. The reactions were initiated by the addition of 0.2 µM antisense ^{32}P-labeled 49-mer oligonucleotide. At the times indicated, the reactions were quenched with an excess of the unlabeled 49-mer oligonucleotide. The DNA substrates and products were deproteinized by a treatment with 0.2% SDS and 1.5 mg/ml proteinase K at 30°C for 10 min. The products were fractionated by 10% PAGE in 0.5× TBE. The gels were dried, exposed to an imaging plate and visualized using an FLA-7000 imaging analyzer (Fujifilm, Tokyo, Japan).

Electron microscopic analysis

The ssDNA catemers formed by EVL and Topo I were extracted by phenol/chloroform and precipitated with ethanol. The ssDNA catemers were then coated with RecA in the absence of ATP and were stained on a copper-plated carbon grid with 2% uranyl acetate. The samples were visualized by tungsten rotary shadowing, and were observed with a JEOL JEM 2000FX electron microscope (JEOL, Akishima, Tokyo, Japan).

Pull-down assays with TOPO IIIα-conjugated beads

Purified human TOPO IIIα was covalently conjugated to Affi-Gel 10 beads (100 µl, Bio-Rad), according to the manufacturer's instructions. To block the remaining active ester sites, ethanolamine (pH 8.0) was added to a final concentration of 100 mM, and the resin was incubated at 4°C overnight. The unbound proteins were removed by washing the Affi-Gel 10-TOPO IIIα beads three times with 500 µl of binding buffer, which contained 20 mM HEPES–NaOH (pH 7.5), 300 mM NaCl, 5 mM 2-mercaptoethanol, 20% glycerol and 0.05% Triton X-100. After washing the resin, the Affi-Gel 10-protein matrices were adjusted to 50% slurries, and were stored at 4°C. The control beads were made by the same method, except that the TOPO IIIα was replaced by the TOPO IIIα storage buffer. For the EVL-binding assay, the TOPO IIIα-beads were incubated with an MCF7 whole-cell extract (1.8 mg of protein), and the beads were washed three times with 200 µl of washing buffer, containing 50 mM Tris–HCl (pH 7.5), 100 mM NaCl, 5 mM EDTA, 0.5% NP-40, 1 mM phenylmethylsulfonyl fluoride and protease inhibitor cocktail (Nacalai Tesque, Kyoto, Japan). The proteins that copelleted with the TOPO IIIα beads were fractionated by 7.5% SDS–PAGE. The EVL protein was detected with the EVL-specific rabbit polyclonal antibodies.

Surface plasmon resonance analysis

The surface plasmon resonance (SPR) signals were measured with a Biacore X100 instrument (GE Healthcare Biosciences, Uppsala, Sweden). Flow cells were maintained at 25°C during the measurement, and the instrument was operated at the mid-flow rate (~30 µl/min). Purified EVL was conjugated to the activated surface of the CM5 sensor chip (GE Healthcare Biosciences, Uppsala, Sweden), using the standard amine coupling conditions recommended by the manufacturer. The level of the conjugated EVL protein was 5600 resonance units. The SPR signals of the flow cell containing a sensor chip without the proteins were subtracted from those of the SPR signals of the flow cell containing the EVL-conjugated sensor chip. The running buffer was 20 mM HEPES–NaOH (pH 7.5), 200 mM NaCl, 2.5% glycerol, 1 mM dithiothreitol and 0.1% Tween-20. For the binding assay, 0.1 µM TOPO IIIα, RPA, Topo I or bovine serum albumin was injected for 2 min.

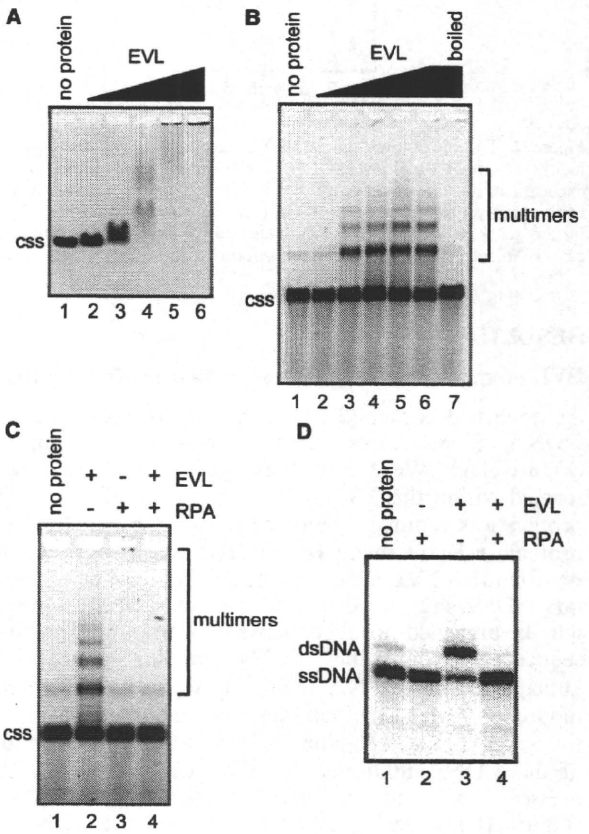

Figure 1. EVL promotes the formation of circular ssDNA multimers. (**A**) The ssDNA-binding assay. ϕX174 ssDNA (20 µM) was incubated with the EVL protein at 37°C for 15 min. The samples were then separated by 0.8% agarose gel electrophoresis in TAE buffer and were visualized by ethidium bromide staining. Lane 1 indicates a negative control experiment without the protein. Lanes 2–6 indicate the experiments with EVL. The concentrations of EVL were 0.1 µM (lane 2), 0.2 µM (lane 3), 0.4 µM (lane 4), 0.8 µM (lane 5) and 1.6 µM (lane 6). The ϕX174 circular ssDNA molecule is indicated by css. (**B**) Multimer formation. ϕX174 circular ssDNA (20 µM) was incubated with EVL. The samples were then separated by 1% agarose gel electrophoresis and were visualized by SYBR Gold staining. The concentrations of EVL were 0.125 µM (lane 2), 0.25 µM (lane 3), 0.5 µM (lane 4), 1 µM (lane 5) and 2 µM (lanes 6 and 7). Lane 7 was incubated at 100°C for 5 min. Lane 1 indicates a negative control experiment without the protein. (**C**) Inhibition of ssDNA multimer formation by RPA. ϕX174 circular ssDNA (20 µM) was incubated with EVL (1 µM) in the presence or absence of RPA (2 µM). (**D**) Inhibition of the EVL-mediated ssDNA annealing by RPA. EVL (1 µM) was first incubated with ssDNA (0.2 µM) in the presence or absence of RPA (80 nM), followed by the addition of a complementary ssDNA. The reactions were conducted at 30°C for 8 min.

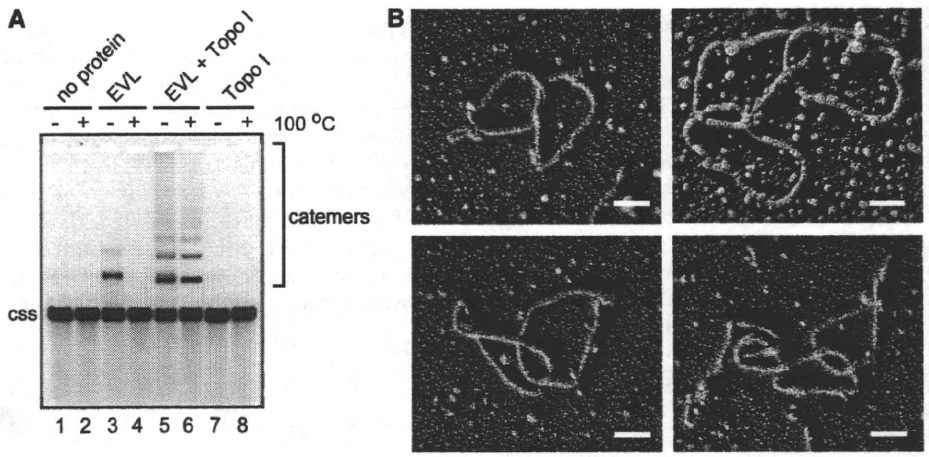

Figure 2. EVL promotes the ssDNA-catenating activity in the presence of Topo I. (**A**) Catemer formation. ϕX174 circular ssDNA (20 μM) was incubated with EVL (1 μM) and Topo I (0.4 nM). Lanes 1 and 2 indicate negative control experiments without the protein. Lanes 3 and 4 indicate the experiments in the presence of EVL. Lanes 5 and 6 indicate the experiments in the presence of EVL and Topo I. Lanes 7 and 8 indicate the experiments in the presence of Topo I. In the experiments shown in lanes 2, 4, 6 and 8, the samples were incubated at 100°C for 5 min before loading on the gel. Lanes 1, 3, 5 and 7 indicate control experiments without the 100°C incubation step. The ϕX174 circular ssDNA molecule is indicated by css. (**B**) Electron microscopic visualization of the ssDNA catemers. Scale bars denote 100 nm.

RESULTS

EVL promotes the formation of circular ssDNA multimers

As described earlier (2), EVL bound to ϕX174 circular ssDNA (5386 bases) and formed large complexes (Figure 1A). We found that ssDNA multimers were formed within this EVL–ssDNA complex, after the EVL protein was removed from the complex by an SDS and proteinase K treatment (Figure 1B). Since we previously reported that EVL promotes the annealing of complementary ssDNAs (2), we suspected that the ssDNA multimers may be annealed products between short, complementary sequences within the ϕX174 circular ssDNA. As anticipated, the ssDNA multimers were dissociated into monomers, when the samples were incubated at 100°C for 5 min (Figure 1B, lane 7). In addition, the formation of the ssDNA multimers by EVL was completely suppressed by an ssDNA-binding protein, RPA (Figure 1C), which significantly inhibited the ssDNA annealing by EVL (Figure 1D). Therefore, we concluded that EVL promotes annealing between short, complementary sequences within the ϕX174 circular ssDNA and forms ssDNA multimers.

EVL promotes ssDNA catenation in the presence of Topo I

The ssDNA multimers formed by EVL may be annealed products, because the multimers were dissociated by heating (Figure 1B). Interestingly, we found that the ssDNA multimers formed by EVL in the presence of a type I topoisomerase, *E. coli* Topo I, were not resolved after incubation at 100°C for 5 min (Figure 2A, lane 6). These heat-stable ssDNA multimers may be ssDNA catemers. To assess whether ssDNA catemers were formed, we visualized the heat-stable ssDNA multimers by electron microscopy. To do so, the ssDNA multimers were purified, and were then coated with RecA to visualize

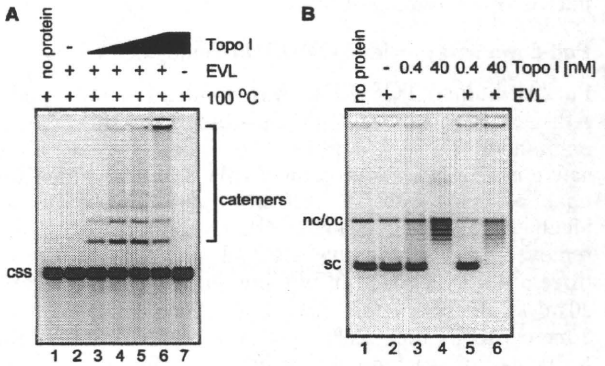

Figure 3. Catalytic function of Topo I in the EVL-mediated ssDNA-catenating reaction. (**A**) ϕX174 circular ssDNA (20 μM) was incubated with Topo I in the presence of EVL. To eliminate the annealed products, the reaction products were treated at 100°C for 5 min before loading on the gel. Lane 1 is a control experiment without the proteins. Lane 2 indicates a negative control experiment without Topo I in the presence of EVL (1 μM). Lanes 3–6 indicate the experiments with various amounts of Topo I in the presence of EVL (1 μM). The concentrations of Topo I are 0.04 nM (lane 3), 0.2 nM (lane 4), 0.4 nM (lane 5) and 0.8 nM (lane 6). Lane 7 indicates a negative control experiment with Topo I (0.8 nM) in the absence of EVL. The ϕX174 circular ssDNA molecule is indicated by css. (**B**) ϕX174 superhelical dsDNA (20 μM) was incubated with EVL (1 μM) and Topo I (0.4 nM or 40 nM). Lane 1 indicates the negative control experiment without the protein. Lanes 2, 5 and 6 indicate the experiments in the presence of EVL (1 μM). Lanes 3 and 5 indicate the experiments in the presence of a low amount of Topo I (0.4 nM). Lanes 4 and 6 indicate the experiments in the presence of a high amount of Topo I (40 nM). ϕX174 superhelical and nicked or open circular dsDNA molecules are indicated by sc and nc/oc, respectively.

the ssDNA. As anticipated, circular ssDNA catemers, containing two or three ssDNA molecules, were observed (Figure 2B). We counted a total of 102 molecules from the DNA samples and found that about 72.5, 18.6, 6.9 and 2% of ssDNA molecules were single circles, two

ssDNA catemers, three ssDNA catemers and four or five ssDNA catemers, respectively. Therefore, we concluded that the heat-stable ssDNA multimers are ssDNA catemers.

The ssDNA-catenating reaction did not occur when either EVL or Topo I was omitted from the reaction mixture (Figure 3A, lanes 2 and 7), indicating that both EVL and Topo I are essential for the ssDNA-catenating reaction. In addition, the formation of EVL-dependent DNA catemers was not detected when circular dsDNA was used as a substrate (Figure 3B). Protein titration experiments revealed that a very small amount of Topo I (0.04 nM) was sufficient to form the ssDNA catemers (Figure 3A, lane 3). This Topo I concentration (0.04 nM) was far below the amount required for inducing a topological change in supercoiled DNA, because 0.4 nM of Topo I is not sufficient to relax supercoiled DNA (Figure 3B, lanes 3 and 5). Therefore, these results suggested that Topo I catalytically functions in the EVL-dependent ssDNA-catenating reaction.

EVL-mediated ssDNA annealing plays an essential role in the ssDNA-catenating reaction

We next tested whether the ssDNA annealing by EVL plays an essential role in the ssDNA-catenating reaction with Topo I. To do so, we prepared two EVL fragments, EVL(1–221) and EVL(222–418), which contained amino acid residues 1–221 and 222–418, respectively (7). As shown in Figure 4A and B, EVL(222–418) promoted annealing to a similar extent as full-length EVL, but EVL(1–221) did not. We then tested whether EVL(1–221) and EVL(222–418) support the ssDNA-catenating reaction. As anticipated, EVL(222–418), which possesses the annealing activity, promoted the ssDNA-catenating reaction, with indistinguishable efficiency from the full-length EVL (Figure 4C, lane 7). In contrast, EVL(1–221) did not promote the ssDNA-catenating reaction (Figure 4C, lane 6). These results indicated that the EVL annealing activity is essential for the ssDNA-catenating reaction with Topo I.

Human TOPO IIIα catalyzes the ssDNA-catenating reaction in the presence of EVL

We then determined whether human topoisomerase can also promote the EVL-dependent ssDNA-catenating reaction. A eukaryotic type I topoisomerase, human TOPO IIIα, reportedly functions in homologous recombination (11–18). Therefore, we purified human TOPO IIIα as a recombinant protein (Figure 5A). The purified TOPO IIIα was chemically conjugated to Affi-Gel 10, and pull-down assays were performed with MCF7 cell extracts. As shown in Figure 5B (lane 3), the endogenous EVL protein in the MCF7 cells was clearly detected in the TOPO IIIα-bound fraction. A SPR analysis also revealed that purified TOPO IIIα efficiently bound to EVL (Figure 5C). We next performed the EVL-dependent ssDNA-catenating assay with TOPO IIIα. As shown in Figure 5D, TOPO IIIα significantly stimulated the ssDNA-catenating reaction in the presence of EVL. Like *E. coli* Topo I (Figure 3A), the ssDNA catemers were

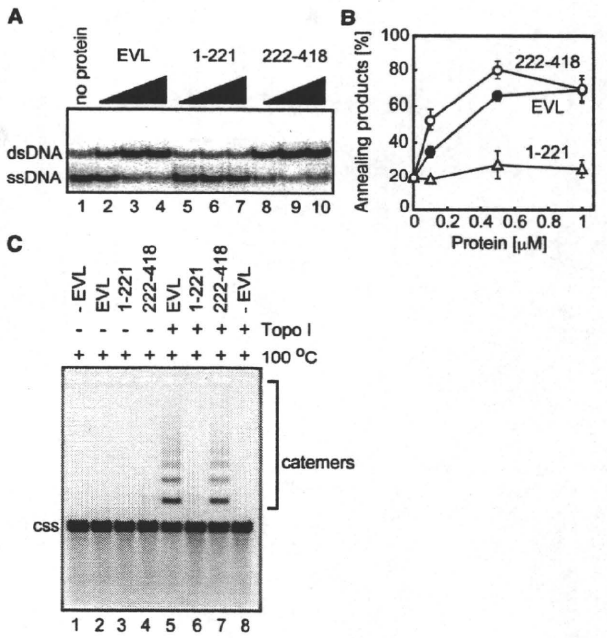

Figure 4. The EVH2 domain is responsible for the ssDNA-annealing activity and the ssDNA-catenation. (**A**) ssDNA annealing activities of EVL(222–418). EVL, EVL(1–221) or EVL(222–418) was first incubated with ssDNA (0.2 μM), followed by the addition of a complementary ssDNA. The reactions were conducted at 30°C for 8 min. Lane 1 indicates a control experiment without protein, and lanes 2–4, lanes 5–7 and lanes 8–10 indicate the experiments with EVL, EVL(1–221) and EVL(222–418), respectively. The EVL, EVL(1–221) and EVL(222–418) concentrations were 0.1 μM (lanes 2, 5 and 8), 0.5 μM (lanes 3, 6 and 9) and 1 μM (lanes 4, 7 and 10). (**B**) Graphical representation of the experiments shown in panel A. The band intensities of the annealed products were quantified, and the average values of three independent experiments are shown with the standard deviation values. Closed circles, open circles and open triangles indicate experiments with EVL, EVL(222–418) and EVL(1–221), respectively. (**C**) Catemer formation with the EVL(222–418) fragment. Lane 1 indicates a control experiment without protein. Lanes 2 and 5 indicate the experiments with EVL. Lanes 3 and 6 indicate the experiments with EVL(1–221). Lanes 4 and 7 indicate the experiments with EVL(222–418). Lanes 5–8 indicate the experiments in the presence of Topo I (0.4 nM). The ϕX174 circular ssDNA molecule is indicated by css.

formed with a very small amount of TOPO IIIα (0.01 nM, Figure 5D, lane 4), suggesting its catalytic function in the reaction. The ssDNA catemers were not formed when either EVL or TOPO IIIα was omitted from the reaction mixture (Figure 5D, lanes 2 and 8). In addition, we found that the ssDNA-catenating reaction mediated by EVL and TOPO IIIα was significantly inhibited by RPA (Figure 6A), which suppresses the EVL-dependent ssDNA annealing (Figure 1C and D). The EVL-TOPO IIIα interaction was still observed in the presence of RPA (Figure 6B). These results suggested that RPA inhibits the ssDNA-catenating reaction by inhibiting the EVL-mediated ssDNA annealing.

Intriguingly, we also found that EVL bound to *E. coli* Topo I, with reduced affinity as compared to human TOPO IIIα *in vitro* (Figure 5C). Although this EVL-Topo I combination does not exist in the natural context, it suggested that EVL binding to the Topo I

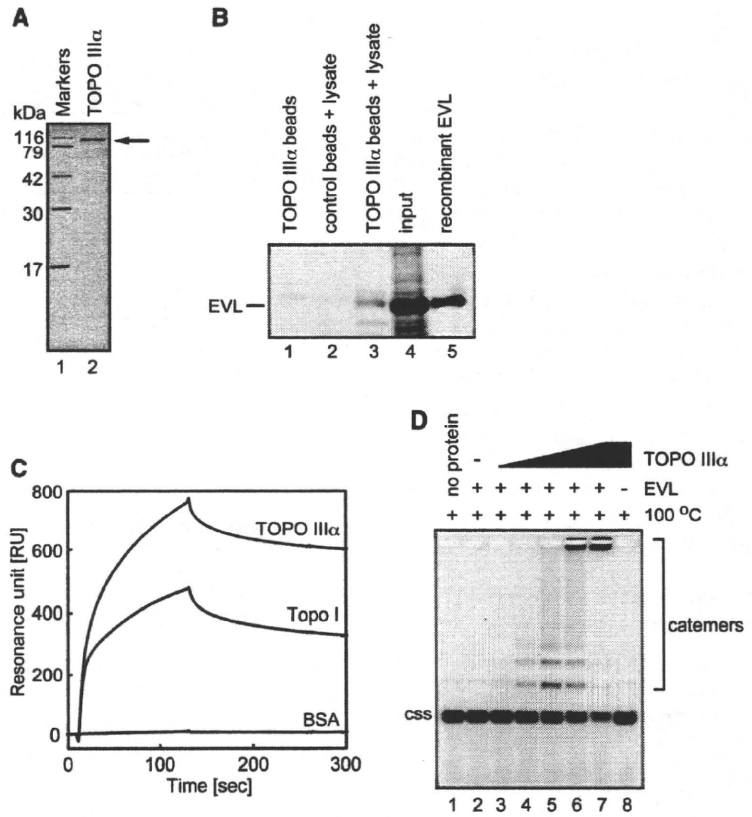

Figure 5. Human TOPO IIIα catalyzes the ssDNA-catenating reaction in the presence of EVL. (**A**) Human TOPO IIIα was purified and analyzed by 15% SDS–PAGE with Coomassie Brilliant Blue staining. (**B**) Pull down assay. Affi-Gel 10 beads chemically conjugated with human TOPO IIIα were incubated with MCF7 whole cell extract. Proteins bound to the TOPO IIIα beads were separated by SDS–PAGE and were analyzed by western blotting. Endogenous EVL was probed with an anti-EVL polyclonal antibody. Lanes 2 and 3 indicate experiments with the control Affi-Gel 10 beads and the TOPO IIIα beads, respectively, in the presence of the MCF7 cell lysate. Lane 1 indicates a control experiment with the TOPO IIIα beads in the absence of the MCF7 cell lysate. The input MCF7 cell lysate (20 μg of protein) and the purified EVL (2 ng) protein were applied in lanes 4 and 5, respectively. (**C**) SPR analysis of the TOPO IIIα-EVL interaction. Sensorgrams for TOPO IIIα, Topo I and bovine serum albumin (BSA) binding to the immobilized EVL protein are presented. (**D**) ϕX174 circular ssDNA (20 μM) was incubated with TOPO IIIα in the presence of EVL. To eliminate the annealed products, the reaction products were treated at 100°C for 5 min before loading on the gel. Lane 1 is a control experiment without the proteins. Lane 2 indicates a negative control experiment without TOPO IIIα in the presence of EVL (1 μM). Lanes 3–7 indicate the experiments with various amounts of TOPO IIIα in the presence of EVL (1 μM). The concentrations of TOPO IIIα are 0.001 nM (lane 3), 0.01 nM (lane 4), 0.05 nM (lane 5), 0.1 nM (lane 6) and 0.5 nM (lane 7). Lane 8 indicates a negative control experiment with TOPO IIIα (0.5 nM) in the absence of EVL. The ϕX174 circular ssDNA molecule is indicated by css.

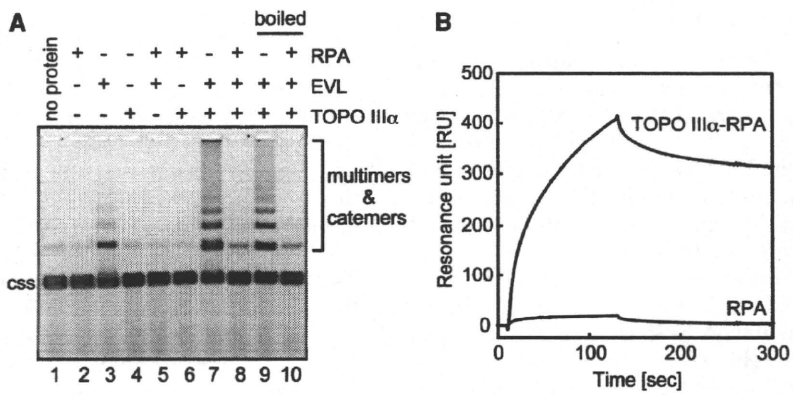

Figure 6. RPA inhibits the ssDNA-catenating reaction mediated by EVL and human TOPO IIIα. (**A**) ϕX174 circular ssDNA (20 μM) was incubated with TOPO IIIα and EVL in the presence or absence of RPA. Lanes 1–8 indicate control experiments without boiling. Lanes 9 and 10 indicate the ssDNA-catenating experiments, in which the reaction products were treated at 100°C for 5 min before loading on the gel. Proteins added to the reactions are indicated on the top of panel A. Protein concentrations were RPA (2 μM), EVL (1 μM) and TOPO IIIα (0.1 nM). (**B**) SPR analysis of the TOPO IIIα–EVL interaction in the presence of RPA. Sensorgrams for TOPO IIIα/RPA and RPA binding to the immobilized EVL protein are presented.

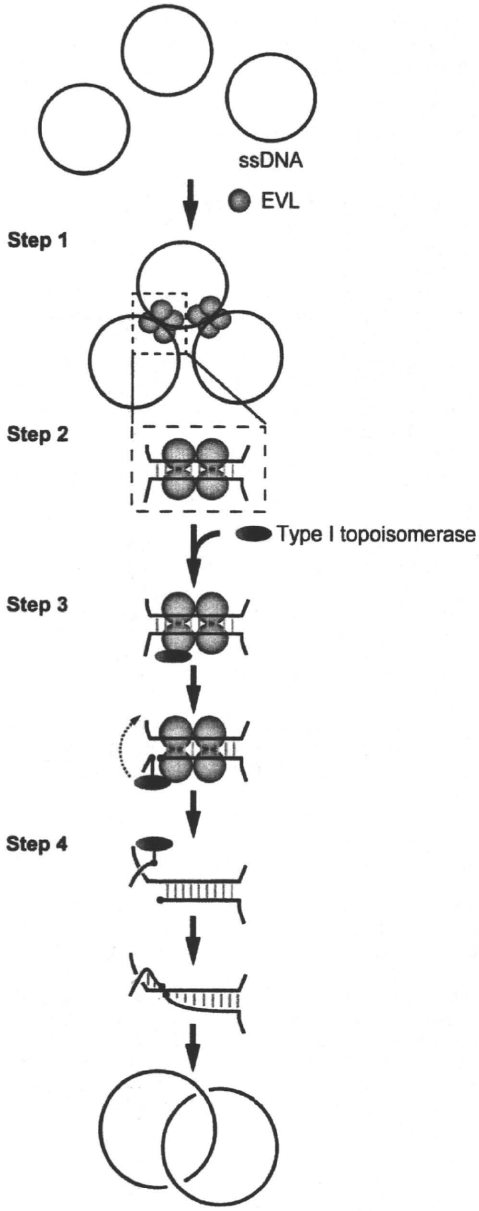

Figure 7. Model for the ssDNA-catenating reaction by EVL and a type I topoisomerase.

region, which may be evolutionarily conserved with TOPO IIIα, may enhance the ssDNA-catenating reaction *in vitro*.

DISCUSSION

In the present study, we found that human EVL and a type I topoisomerase promote the catenation of ssDNA molecules. It has been reported that RecA, a bacterial recombinase, promotes hemicatenation between ssDNA and dsDNA in the presence of Topo I (8); however, no report for the ssDNA-catenating reaction has been published thus far. We also confirmed that both prokaryotic and eukaryotic type I topoisomerases are functional for the ssDNA catenation with EVL.

Type I topoisomerase promotes cutting and rejoining reactions on a strand within dsDNA. In the present study, we showed that the annealing activity of EVL plays an essential role in the ssDNA-catenating reaction with a type I topoisomerase. Therefore, we have proposed an annealing-mediated model for the ssDNA-catenating reaction (Figure 7). In this model, EVL first binds to ssDNA and forms large complexes, each containing multiple ssDNA molecules (Step 1). Since human EVL contains a tetramerization domain at its C-terminus (21), the formation of multiple ssDNA complexes may be mediated through its tetramerization activity. The short complementary sequences of the ssDNA may be annealed within the EVL-multiple ssDNA complexes (Step 2). A type I topoisomerase, which may be recruited on the ssDNA annealed sites through binding to EVL, then cuts an ssDNA strand within the annealed region (Step 3). This nicked site rotates and rejoins (Step 4).

The functional significance of the ssDNA catenation by EVL and topoisomerases remains to be elucidated; however, it may be involved in homologous recombination because EVL directly interacts with the eukaryotic RecA homologs, RAD51 and RAD51B (2). Our previous analyses suggested that EVL may function as a RAD51 mediator, which stimulates the RAD51-mediated homologous-pairing and strand-exchange reactions (2,7). The ssDNA-catenating activity, comprising the ssDNA cutting and rejoining reactions, may be utilized to process the DNA intermediates formed by the homologous-pairing and strand-exchange reactions by RAD51. In the homologous-recombination process, it has been proposed that a DNA intermediate containing a D-loop, in which the ssDNA has invaded a homologous region of the intact dsDNA, is first formed by the RAD51-mediated homologous pairing. After this homologous-pairing step, the invading strand primes repair synthesis of the DNA strands, and the D-loop structure is converted to a four-way junction, the Holliday-junction intermediate, which moves along the DNA to expand the newly paired heteroduplex region. The ssDNA cutting and rejoining activities of EVL and topoisomerase may be involved in the conversion process from the D-loop to Holliday junction intermediates.

Alternatively, the ssDNA cutting and rejoining activities may function in the resolution of the Holliday junction. The Holliday-junction intermediate must be resolved into two parental DNA molecules by the ssDNA-nicking activity in the late stage of the homologous-recombination pathway. Interestingly, human TOPO IIIα, which was found to promote the ssDNA-catenating reaction with EVL, is reportedly involved in Holliday junction dissolution (13–16). In addition, EVL is known to bind RAD51B, which preferentially binds to the Holliday junction (2,22). Therefore, EVL may also be involved in the late stage of the HRR pathway, together with TOPO IIIα. Further analyses are required to clarify these issues.

ACKNOWLEDGEMENT

H. K. is a research fellow in the Waseda Research Institute for Science and Engineering.

FUNDING

Grants-in-Aid from the Ministry of Education, Culture, Sports, Science and Technology (MEXT), and the Japanese Society for the Promotion of Science (JSPS) of Japan. Funding for open access charge: Waseda University.

Conflict of interest statement. None declared.

REFERENCES

1. Kwiatkowski,A.V., Gertler,F.B. and Loureiro,J.J. (2003) Function and regulation of Ena/VASP proteins. *Trends Cell. Biol.*, **13**, 386–392.
2. Takaku,M., Machida,S., Hosoya,N., Nakayama,S., Takizawa,Y., Sakane,I., Shibata,T., Miyagawa,K. and Kurumizaka,H. (2009) Recombination activator function of the novel RAD51- and RAD51B-binding protein, human EVL. *J. Biol. Chem.*, **284**, 14326–14336.
3. Symington,L.S. (2002) Role of RAD52 epistasis group genes in homologous recombination and double-strand break repair. *Microbiol. Mol. Biol. Rev.*, **66**, 630–670.
4. West,S.C. (2003) Molecular views of recombination proteins and their control. *Nat. Rev. Mol. Cell. Biol.*, **4**, 435–445.
5. Sung,P., Krejci,L., Van Komen,S. and Sehorn,M.G. (2003) Rad51 recombinase and recombination mediators. *J. Biol. Chem.*, **278**, 42729–42732.
6. San Filippo,J., Sung,P. and Klein,H. (2008) Mechanism of eukaryotic homologous recombination. *Annu. Rev. Biochem.*, **77**, 229–257.
7. Takaku,M., Machida,S., Nakayama,S., Takahashi,D. and Kurumizaka,H. (2009) Biochemical analysis of the human EVL domains in homologous recombination. *FEBS J.*, **276**, 5841–5848.
8. Cunningham,R.P., Wu,A.M., Shibata,T., DasGupta,C. and Radding,C.M. (1981) Homologous pairing and topological linkage of DNA molecules by combined action of *E. coli* RecA protein and topoisomerase I. *Cell*, **24**, 213–223.
9. Harmon,F.G., DiGate,R.J. and Kowalczykowski,S.C. (1999) RecQ helicase and topoisomerase III comprise a novel DNA strand passage function: a conserved mechanism for control of DNA recombination. *Mol. Cell*, **3**, 611–620.
10. Harmon,F.G., Brockman,J.P. and Kowalczykowski,S.C. (2003) RecQ helicase stimulates both DNA catenation and changes in DNA topology by topoisomerase III. *J. Biol. Chem.*, **278**, 42668–42678.
11. Wu,L., Davies,S.L., North,P.S., Goulaouic,H., Riou,J.F., Turley,H., Gatter,K.C. and Hickson,I.D. (2000) The Bloom's syndrome gene product interacts with topoisomerase III. *J. Biol. Chem.*, **275**, 9636–9644.
12. Cheok,C.F., Bachrati,C.Z., Chan,K.L., Ralf,C., Wu,L. and Hickson,I.D. (2005) Roles of the Bloom's syndrome helicase in the maintenance of genome stability. *Biochem. Soc. Trans.*, **33**, 1456–1459.
13. Wu,L. and Hickson,I.D. (2003) The Bloom's syndrome helicase suppresses crossing over during homologous recombination. *Nature*, **426**, 870–874.
14. Wu,L., Bachrati,C.Z., Ou,J., Xu,C., Yin,J., Chang,M., Wang,W., Li,L., Brown,G.W. and Hickson,I.D. (2006) BLAP75/RMI1 promotes the BLM-dependent dissolution of homologous recombination intermediates. *Proc. Natl Acad. Sci. USA*, **103**, 4068–4073.
15. Raynard,S., Bussen,W. and Sung,P. (2006) A double Holliday junction dissolvasome comprising BLM, topoisomerase IIIalpha, and BLAP75. *J. Biol. Chem.*, **281**, 13861–13864.
16. Bussen,W., Raynard,S., Busygina,V., Singh,A.K. and Sung,P. (2007) Holliday junction processing activity of the BLM-Topo IIIalpha-BLAP75 complex. *J. Biol. Chem.*, **282**, 31484–31492.
17. Raynard,S., Zhao,W., Bussen,W., Lu,L., Ding,Y.Y., Busygina,V., Meetei,A.R. and Sung,P. (2008) Functional role of BLAP75 in BLM-topoisomerase IIIalpha-dependent holliday junction processing. *J. Biol. Chem.*, **283**, 15701–15708.
18. Singh,T.R., Ali,A.M., Busygina,V., Raynard,S., Fan,Q., Du,C.H., Andreassen,P.R., Sung,P. and Meetei,A.R. (2008) BLAP18/RMI2, a novel OB-fold-containing protein, is an essential component of the Bloom helicase-double Holliday junction dissolvasome. *Genes Dev.*, **22**, 2856–2868.
19. Henricksen,L.A., Umbricht,C.B. and Wold,M.S. (1994) Recombinant replication protein A: expression, complex formation, and functional characterization. *J. Biol. Chem.*, **269**, 11121–11132.
20. Bradford,M.M. (1976) A rapid and sensitive method for the quantitation of microgram quantities of protein utilizing the principle of protein-dye binding. *Anal. Biochem.*, **72**, 248–254.
21. Bachmann,C., Fischer,L., Walter,U. and Reinhard,M. (1999) The EVH2 domain of the vasodilator-stimulated phosphoprotein mediates tetramerization, F-actin binding, and actin bundle formation. *J. Biol. Chem.*, **274**, 23549–23557.
22. Yokoyama,H., Kurumizaka,H., Ikawa,S., Yokoyama,S. and Shibata,T. (2003) Holliday junction binding activity of the human Rad51B protein. *J. Biol. Chem.*, **278**, 2767–2772.

THE JOURNAL OF BIOLOGICAL CHEMISTRY VOL. 285, NO. 38, pp. 29662–29670, September 17, 2010

Ataxia Telangiectasia Mutated (ATM)-mediated DNA Damage Response in Oxidative Stress-induced Vascular Endothelial Cell Senescence*[S]

Received for publication, March 24, 2010, and in revised form, July 15, 2010 Published, JBC Papers in Press, July 16, 2010, DOI 10.1074/jbc.M110.125138

Hong Zhan[‡1], **Toru Suzuki**[‡§1,2], **Kenichi Aizawa**[‡§1], **Kiyoshi Miyagawa**[¶], **and Ryozo Nagai**[‡3]

From the Departments of [‡]*Cardiovascular Medicine,* [§]*Ubiquitous Preventive Medicine, and* [¶]*Radiation Biology, Graduate School of Medicine, The University of Tokyo, 7-3-1 Hongo, Bunkyo, Tokyo 113-8655, Japan*

Oxidative stress regulates dysfunction and senescence of vascular endothelial cells. The DNA damage response and its main signaling pathway involving ataxia telangiectasia mutated (ATM) have been implicated in playing a central role in mediating the actions of oxidative stress; however, the role of the ATM signaling pathway in vascular pathogenesis has largely remained unclear. Here, we identify ATM to regulate oxidative stress-induced endothelial cell dysfunction and premature senescence. Oxidative stress induced senescence in endothelial cells through activation/phosphorylation of ATM by way of an Akt/p53/p21-mediated pathway. These actions were abrogated in cells in which ATM was knocked down by RNA interference or inhibited by specific inhibitory compounds. Furthermore, the *in vivo* significance of this regulatory pathway was confirmed using ATM knock-out mice in which induction of senescent endothelial cells in the aorta in a diabetic mouse model of endothelial dysfunction and senescence was attenuated in contrast to pathological changes seen in wild-type mice. Collectively, our results show that ATM through an ATM/Akt/p53/p21-dependent signaling pathway mediates an instructive role in oxidative stress-induced endothelial dysfunction and premature senescence.

The DNA damage response is activated in response to stimuli ranging from oxidative stress, oncogenic stress to ionizing radiation to determine which cells remain viable after cytopathogenic insult. Recent reports suggest that the DNA damage response in addition to its classical role in regulating the cell cycle checkpoint in cancer to also play a major regulatory role in nononcogenic fields such as in aging/senescence (1–3). One field in which the DNA damage response has remained poorly addressed is the cardiovasculature.

Aging is known to be a major cardiovascular risk factor (4). Premature senescence in endothelial cells is induced by proatherogenic and proinflammatory factors such as hydrogen peroxide (H_2O_2), oxidized LDL or TNF-α by telomeric inactivation through an Akt-dependent mechanism (5, 6). Because regulation of aging/senescence of the vasculature, notably through the endothelial cell, contributes to mechanisms of arteriosclerosis and other age-related cardiovascular diseases (7), we questioned whether the DNA damage response might play a role in regulation of endothelial regulation of aging/senescence. For this, we focused on the role of ataxia telangiectasia mutated (ATM),[4] which is the central effector molecule in the DNA damage response pathway.

ATM belongs to the phosphoinositide 3-kinase (PI3-kinase)-related protein kinase (PIKK) family which has been identified as the product mutated or inactivated in ataxia telangiectasia (A-T) patients. The DNA damage response and its main signaling pathway involving ATM have been implicated in playing a central role in mediating the actions of oxidative stress (8–10). However, the role of the ATM signaling pathway in vascular pathogenesis has remained unclear. Further, pathogenic mechanisms of the vascular pathologies associated with mutated ATM (telangiectasia, premature coronary artery disease) remain obscure.

In the present study, we examined the effects of ATM-mediated oxidative stress-induced senescence in vascular pathologies through actions on endothelial cells. Our results show that ATM through an ATM/Akt/p53/p21-dependent signaling pathway mediates an instructive role in oxidative stress-induced endothelial dysfunction and premature senescence.

EXPERIMENTAL PROCEDURES

Cell Culture—Human umbilical vein endothelial cells (HUVECs) were purchased from Sanko Junyaku (Tokyo, Japan) and maintained with endothelial cell basal medium-2 containing EGM-2 supplement as purchased from Cambrex Bio Science (Rockland, MD) in humidified air with 5% CO_2 at 37 °C. All experiments were performed between passages 4 and 6.

Western Blot Analysis and Antibodies—HUVECs (3×10^5 cells/well) were treated with 100 μM H_2O_2 in the absence or presence of *N*-acetyl-L-cysteine (NAC) (Sigma-Aldrich), caffeine (Wako, Osaka, Japan), or KU-55933 (Calbiochem). Cells were washed with cold phosphate-buffered saline (PBS) and

* This work was supported by grants-in-aid for scientific research (T. S., K. A., and R. N.) from the Ministry of Education, Culture, Sports, Science, and Technology, Japan.

[S] The on-line version of this article (available at http://www.jbc.org) contains supplemental Experimental Procedures and Figs. 1–7.

[1] These authors contributed equally to this work.

[2] To whom correspondence may be addressed: Dept. of Cardiovascular Medicine, Graduate School of Medicine, The University of Tokyo, 7-3-1 Hongo, Bunkyo, Tokyo 113-8655, Japan. Tel.: 81-3-5800-9846; Fax: 81-3-5800-9847; E-mail: torusuzu-tky@umin.ac.jp.

[3] To whom correspondence may be addressed. Tel.: 81-3-5800-6526; Fax: 81-3-3815-2087; E-mail: nagai-tky@umin.ac.jp.

[4] The abbreviations used are: ATM, ataxia telangiectasia mutated; A-T, ataxia telangiectasia; BisTris, bis(2-hydroxyethyl)iminotris(hydroxymethyl)methane; DSB, DNA double-strand break; HUVEC, human umbilical vein endothelial cell; NAC, *N*-acetyl-L-cysteine; SA-β-gal, senescence-associated β-galactosidase; STZ, streptozotocin.

lysed with 2× NuPAGE LDS sample buffer (Invitrogen) supplemented with 1 mM sodium orthovanadate (Sigma-Aldrich) and 1 mM sodium fluoride (Wako). Lysates were then boiled for 10 min and centrifuged for 2 min at 4 °C. Equal amounts of protein were separated by NuPAGE 3–8% Tris acetate mini gel electrophoresis or NuPAGE 10% BisTris gel (Invitrogen) and then transferred onto a polyvinylidine difluoride (PVDF) membrane (Invitrogen). Membranes were blocked with 5% skim milk in PBS at room temperature for 1 h and then subsequently probed with primary antibodies at a predetermined optimal concentration for 2–4 h at room temperature or overnight at 4 °C. After rinsing with TBS containing 0.1% Triton X-100 (TBS-T), membranes were incubated with appropriate horseradish peroxidase-conjugated anti-rabbit (Cell Signaling Technology) or anti-mouse IgG (GE Healthcare) for 1 h at room temperature. After three washes with TBS-T, immunoblots were detected using the ECL Plus Western blotting Detection System (GE Healthcare) and exposed to x-ray film (Fuji medical x-ray film, Tokyo, Japan). Anti-phospho-ATM (Ser^{1981}) antibody was purchased from Millipore; anti-ATM (2C1) and anti-p53 (DO-1) antibodies were from Santa Cruz Biotechnology (Santa Cruz, CA); and anti-phospho-p53 (Ser^{15}), anti-phospho-Akt (Ser^{473}), and anti-Akt antibodies were from Cell Signaling Technology. Anti-GAPDH antibody (Life Technologies) was used as a loading control. Purified mouse anti-p21 antibody was obtained from BD Pharmingen. See also supplemental Experimental Procedures.

Immunofluorescence Microscopy—Cells were grown on coverslips at a density of 1×10^5 per slide. After treatment with 100 μM H_2O_2 for 1 h, cells were fixed in 3% paraformaldehyde in PBS for 10 min. Chamber slides were washed three times with PBS and then permeabilized with 0.25% Triton X-100 in PBS for 10 min. After washing twice with PBS and blocking for 5 min with 0.1% gelatin, slides were incubated with primary antibody (1:100) in 0.1% gelatin in PBS for 1 h in a humidified chamber at 37 °C. Cells were blocked three times with 0.1% gelatin, and then samples were incubated with secondary antibody using Alexa Fluor 488 green or Alexa Fluor 635 red (Life Technologies) in 0.1% gelatin in PBS for 1 h in a humidified chamber at 37 °C. Antibodies used for immunofluorescence were ATM-Ser^{1981}, ATM, p53-Ser^{15}, p53, p21, and 53BP1 (Cell Signaling Technology). Nuclei were stained with Hoechst 33258 and mounted with DakoCytomation Fluorescent Mounting Medium (Dako Japan, Kyoto, Japan) and then visualized with a Carl Zeiss LSM510 confocal microscope (Carl Zeiss, Jena, Germany).

Senescence-induced by Oxidative Stress and Senescence-associated β-Galactosidase (SA-β-gal) Staining—Methods for inducing premature senescence by H_2O_2 (Wako) have been described previously (11). Briefly, HUVECs (3×10^5 cells/well) were grown in 30-mm collagen-coated dishes to 80% confluence. Cells were pretreated for 3 days with vehicle, NAC (0.1, 2, and 10 mM), caffeine (0.1, 2, and 5 mM), or KU-55933 (0.5, 5, and 10 μM). After washing three times with endothelial cell basal medium-2 and treating for 1 h with 100 μM H_2O_2, cells were trypsinized, reseeded at a density of 5×10^4 in 30-mm dishes, and cultured with endothelial cell basal medium-2 containing compound for 10 days. Cells were then washed in PBS and fixed for 5 min at room temperature in 2% formaldehyde/0.2% glutaraldehyde, washed, and then incubated at 37 °C for 12 h (without CO_2) with fresh SA-β-gal stain solution which contained 1 mg/ml 5-bromo-4-chloro-3-indolyl-β-D-galactoside (X-Gal), 40 mM citric acid/sodium phosphate, pH 6.0, 5 mM potassium ferrocyanide, 5 mM potassium ferricyanide, 150 mM sodium chloride, and 2 mM magnesium chloride. Senescent cells were identified as blue-stained cells by phase contrast microscopy, and a total of 1,000 cells were counted in 20 random fields to determine the percentage of SA-β-gal-positive cells.

RNA Interference—Small interference RNA (siRNA) constructs were obtained as siGENOME SMARTpool reagent from Dharmacon. See also supplemental Experimental Procedures. A siRNA pool specific for ATM (siGENOME SMARTpool Human ATM, M-003201020005) and control siRNA (siGENOME nontargeting siRNA pool, D-0012061320) were used. HUVECs (3×10^5 cells/well) were grown to 80% confluence in 6-well culture dishes. Transient transfections of 10, 50, and 100 pmol of ATM siRNA or nontarget siRNA were performed by a liposome-mediated method using Lipofectamine 2000 according to the manufacturer's instructions (Invitrogen). The indicated amounts of siRNA and 5 μl of Lipofectamine 2000 were, respectively, diluted in 0.25 ml of Opti-MEM without serum. After incubation for 5 min, diluted siRNA and Lipofectamine 2000 were combined, and the mixture was incubated for 20 min at room temperature to allow the DNA-Lipofectamine 2000 complexes to form. 0.5 ml of complex was added to each well. After 5 h of transfection, the medium with complexes was removed, and endothelial cell basal medium-2 supplemented with EGM-2 was added. At 72 h following transient transfection, total RNA was extracted and submitted to reverse transcription-PCR (RT-PCR) experiments using oligonucleotide primers specific to ATM and 18 S rRNA. In ATM knock-down cells, the levels of total ATM, phospho-p53 (Ser^{15}), phospho-Akt (Ser^{473}), total Akt, or GAPDH proteins were analyzed by Western blotting, or SA-β-gal activity was measured.

RNA Extraction and Quantitative RT-PCR—Total RNA from HUVECs (3×10^5 cells/well) was extracted by the RNeasy Mini kit (Qiagen) according to the manufacturer's instructions. RNA concentration and purity were determined on a spectrophotometer (Ultrospec 3000; GE Healthcare) by calculating the ratio of optical density at 260 nm to 280 nm. One microgram of total RNA sample was used to generate first-strand complementary DNA by using powerscript reverse transcriptase (Clontech) according to the manufacturer's recommended procedures. PCR was then performed for ATM from the same complementary DNA samples using HotStarTaq (Qiagen), 10× PCR buffer, and 2.5 mM dNTP mix. The forward primer 5′-GATGTTGTTGTCCCTACTATGG-3′ and the reverse primer 5′-GCTACACTGCGCGTATAAGCC-3′ corresponded to human ATM. 18 S rRNA (Life Technologies) was used as an internal control. Amplification was initiated by 15 min of denaturation at 95 °C for 1 cycle followed by 30 cycles at 95 °C for 30 s, 57 °C for 30 s, and 72 °C for 40 s. After the last cycle of amplification, samples were incubated at 72 °C for 10 min in a GeneAmp™ PCR system (Applied Biosystems). PCR products, a 589-bp ATM fragment and a 350-bp 18 S fragment, were then visualized by UV

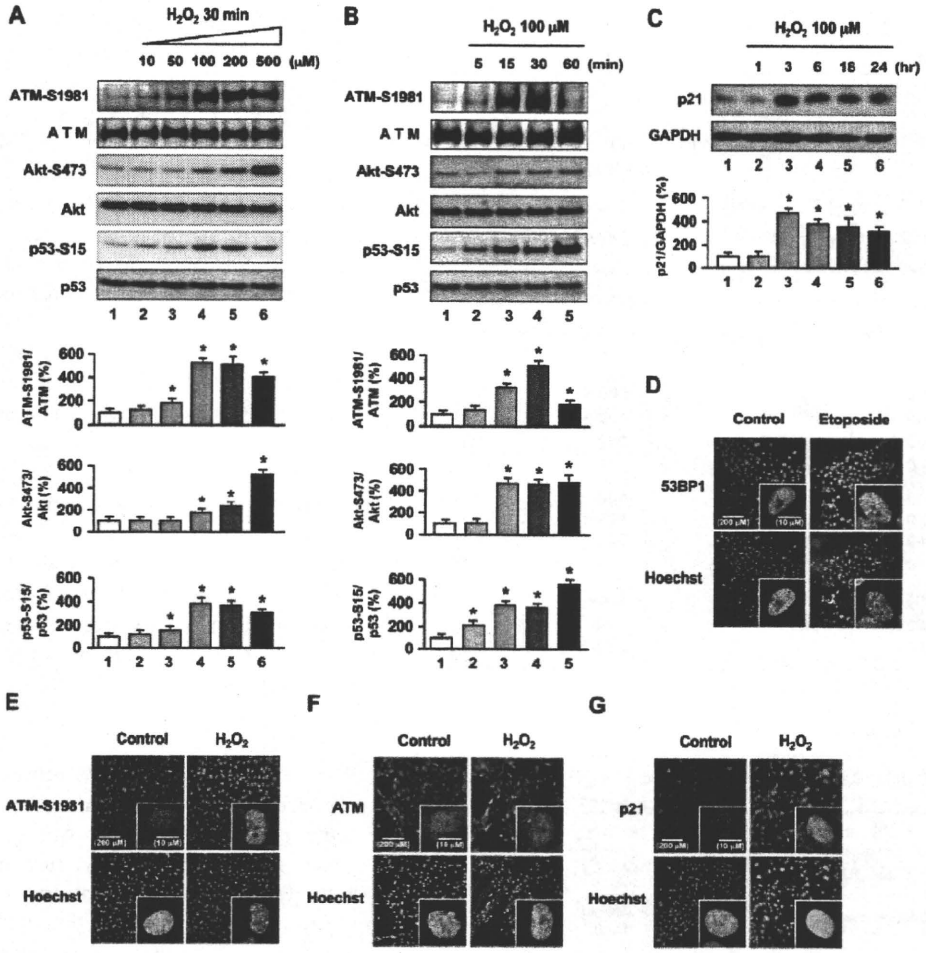

FIGURE 1. **Oxidative stress induces ATM-S1981, Akt-S473, p53-S15 phosphorylation and up-regulation of p21 expression in HUVECs.** *A*, cells were incubated with H_2O_2 for 30 min at the indicated concentrations. *B* and *C*, HUVECs were incubated in 100 μM H_2O_2 for the indicated times. Cells were lysed and subjected to Western blot analyses with the indicated antibodies. GAPDH was used as loading control. Values are mean ± S.E. (*error bars*) ($n = 3$). *, $p < 0.05$ *versus* cells incubated without H_2O_2 treatment. Representative blots are shown in the *upper panels* whereas corresponding quantitation is shown in the *lower panels*. *D–F*, immunofluorescence for 53BP1, phosphorylated ATM-S1981, and total ATM is shown. Cells were exposed to 10 μM etoposide or 100 μM H_2O_2 for 1 h and then immunostained for 53BP1 (*D*), ATM-S1981 (*E*) and total ATM (*F*). Cells incubated without etoposide or H_2O_2 were used as controls. *G*, cells were exposed to 100 μM H_2O_2 for 3 h and then immunostained for p21. Hoechst 33258 was used as nuclear stain (*blue*). Original magnification, ×200 and ×630. *Scale bars*, 200 μm and 10 μm, respectively. Treatment with etoposide and immunofluorescence for 53BP1 (labeled by green fluorescence) was used for a positive control. Expression of phosphorylated ATM-S1981) and p21 labeled by red fluorescence in HUVECs and foci formation was significantly increased after H_2O_2 treatment. Additional views of the photographs are shown in supplemental Fig. 1.

illumination after electrophoresis by 2% agarose gels containing 0.5 μg/ml ethidium bromide.

Animal Experiments—ATM knock-out mice (129S6/SvEvTac-*Atm*^{tm1Awb}/J) were obtained from Jackson Laboratories. All generations were from matings of heterozygous parents. The following sequence, as recommended by Jackson Laboratories, was used for genotyping: oIMR640, 5′-GCTGCCATACTTGATCAATG-3′; oIMR641, 5′-TCCGAATTTGCAGGAGTG-3′; oIMR0013, 5′-CTTGGGTGGAGAGGCTATTC-3; and oIMR0014, 5′-AGGTGAGATGACAGGAGATC-3′. Age-matched 10-week-old SPF male ATM wild-type ($^{+/+}$), heterozygote ($^{+/-}$), and homozygote ($^{-/-}$) mice ($n = 6$, respectively, weighing ~15–25 g) were used. Hyperglycemia was induced by a single intraperitoneal injection of streptozotocin (STZ) (180 mg/kg; Sigma-Aldrich). Tail blood glucose was assayed 3 days after injection using glucose test strips (Roche Applied Science). All diabetic animals had blood glucose values >300 mg/dl. Mice were housed under constant temperature (23 ± 1 °C) with a 12-h light and 12-h dark cycle for 10 days with free access to water and chow and were killed by cervical dislocation. The aorta was removed after systemic perfusion with PBS for histological examination. The aorta was fixed for 30 min at room temperature in 2% formaldehyde/0.2% glutaraldehyde, washed, incubated at 37 °C for 24 h (without CO_2) with fresh SA-β-gal stain solution, and then embedded in OTC compound before freezing in liquid nitrogen. The samples were stored at −80 °C until sample slides were prepared. The proportion of SA-β-gal-positive cells were analyzed by Scion Image software. Serial cross-sections (10 μm) were obtained from each sample and stained with kernechtrot staining solution (Muto, Tokyo, Japan) or prepared for immunohistochemistry. All experimental protocols complied with the guidelines for animal experiments of the University of Tokyo.

Tissue Protein Extraction—Thoracic aorta of ATM knock-out mice ($ATM^{+/+}$, $ATM^{+/-}$, $ATM^{-/-}$ mice) were dissected out of their thoracic aortas and snap frozen in liquid nitrogen. After thawing on ice, the thoracic aortas were homogenized mechanically at 25 Hz for 25 s five times on ice in 150 μl of RIPA buffer (0.1% SDS, 0.5% Nonidet P-40, 0.1% sodium deoxycholate, 150 mM NaCl, 50 mM Tris-HCl, pH 7.9, and 1× EDTA-free complete proteinase inhibitor (Roche Applied Science)). Samples were lysed gently on ice for 30–60 min, and cellular debris was removed by centrifugation. Protein was then quantified using the BCA protein assay kit (Thermo). A 30-μg aliquot of total protein was analyzed for ATM protein by Western blot analysis. Anti-GAPDH antibody was used as a loading control.

Immunohistochemistry—Immunostaining was performed using the Envision kit (Dako Japan). Frozen sections, 10 μm thick, were fixed in acetone at 4 °C, washed in TBS, and then blocked by 0.03% hydrogen peroxidase in methanol. After blocking nonspecific antibody-binding sites, the sections were incubated for 1 h with antibodies against von Willebrand factor (1:1,000; Abcam), p21 and p16 (Santa Cruz Biotechnology) as the primary antibody and then for 1 h with the peroxidase-

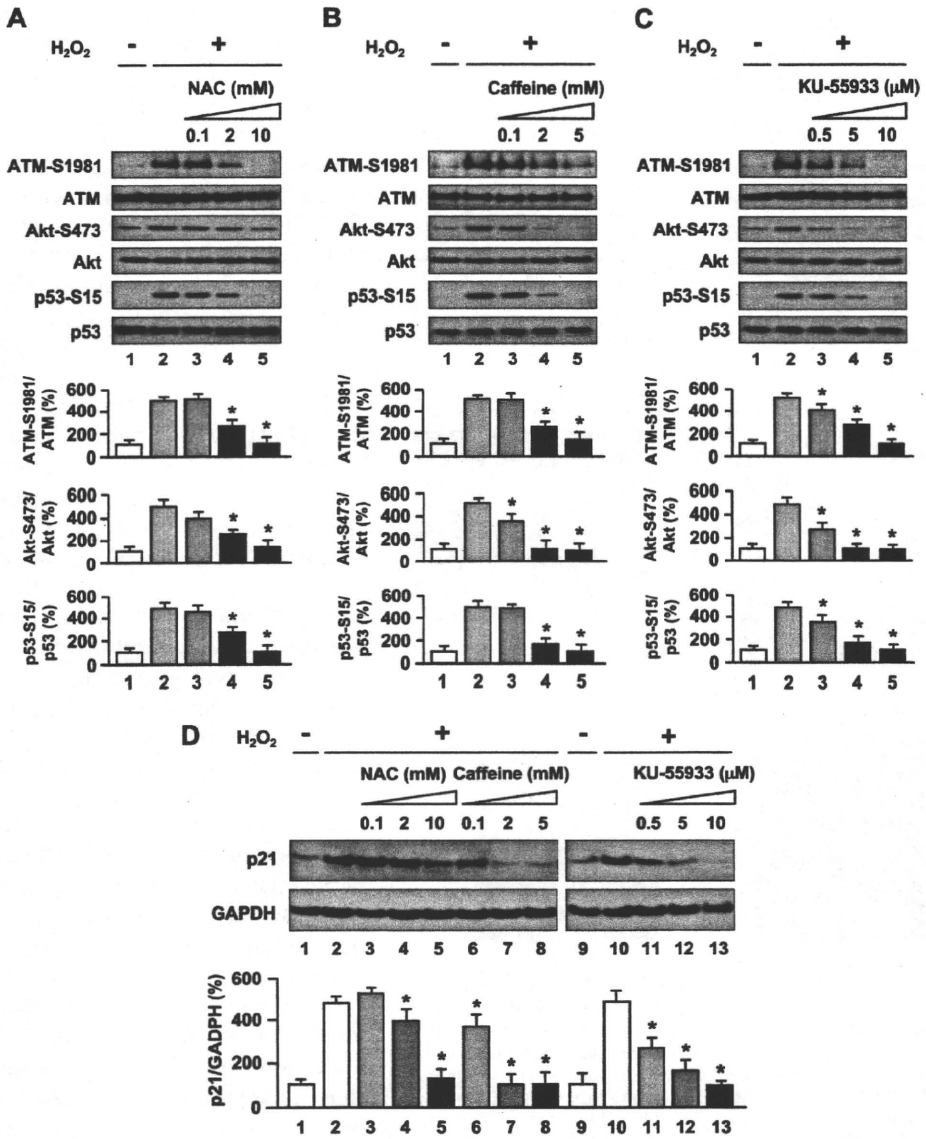

FIGURE 2. **Oxidative stress-induced Akt and p53 phosphorylation and up-regulation of p21 expression are dependent on ATM kinase.** *A–C*, antioxidant and ATM inhibitors blocked phosphorylation of ATM-S1981, Akt-S473, and p53-S15 as stimulated by H_2O_2 exposure. Cells were treated with 100 μM H_2O_2 for 30 min in the absence or presence of NAC (*A*) or caffeine (*B*), or KU-55933 (*C*), and whole cell lysates were subjected to Western blot analyses using the indicated antibodies. *D*, antioxidant and ATM inhibitors down-regulated p21 induction as stimulated by H_2O_2 exposure. Cells were pretreated with NAC, caffeine, or KU-55933 and then 100 μM H_2O_2 for 3 h. Whole cell lysates were subjected to Western blot analyses using p21 antibody. GAPDH was used as loading control. Values are mean ± S.E. (*error bars*) ($n = 3$). *, $p < 0.05$ *versus* cells incubated with H_2O_2. Representative blots are shown in the *upper panels* whereas corresponding quantitation is shown in the *lower panels*.

vation and expression of ATM in cultured HUVECs treated with H_2O_2 as an inducing agent of oxidative stress. HUVECs exposed to H_2O_2 showed increased ATM phosphorylation at Ser^{1981} (ATM-S1981) (Fig. 1, *A* and *B*), which releases it from an inhibitory homodimer structure leading to its activation and recruitment to sites of DNA double-strand breaks (DSBs) (12–14). We next investigated factors involved in the ATM signaling pathway. Because ATM mediates activation of Akt in response to insulin or ionizing radiation which then in turn results in radiosensitivity or resistance to insulin in cell lines derived from A-T patients and ATM knock-out mice (15), we first investigated the activation of Akt in response to oxidative stress. Akt phosphorylation at Ser^{473} (Akt-S473) was increased in H_2O_2-treated HUVECs (Fig. 1, *A* and *B*). We then investigated involvement of p53, a downstream signaling molecule of ATM (10) and Akt (6), which showed phosphorylation at Ser^{15} (p53-S15) after exposure to H_2O_2 (Fig. 1, *A* and *B*). Furthermore, p21, a downstream target of p53, was increased in H_2O_2-treated HUVECs (Fig. 1*C*). Our results indicate that oxidative stress phosphorylates ATM and its involved genes, Akt and p53, with subsequent up-regulation of p21 expression. Thus, the phosphorylation of ATM, Akt, and p53 and up-regulation of p21 expression mediate actions of oxidative stress in endothelial cells.

Although ATM is predominantly present in the nucleus, a variable amount (<10%) has been reported in the cytoplasm, especially in neuronal cells. The major known role of nuclear ATM is to participate in the response to DSBs for DNA repair and cell cycle checkpoint activation (16). In response to agents that induce DSBs, ATM has been found to relocalize to the sites of breaks and in doing so forms large nuclear foci (17). To determine whether oxidative stress-induced ATM forms foci, immunofluorescence analyses for phospho-ATM (Ser^{1981}), total ATM, and p21 were performed. Increased fluorescence and foci formation were seen in response to H_2O_2 for phosphorylated ATM (Fig. 1*E* and supplemental Fig. 1*B*) and increased p21 (Fig. 1*G* and supplemental Fig. 1*D*) under conditions in which 53BP1 formed nuclear foci in response to etoposide as reported

labeled polymer. Finally, sections were incubated with diaminobenzidine tetrahydrochloride (Dako Japan), and the nuclei were counterstained with hematoxylin.

Statistical Analysis—All values are expressed as mean ± S.E. Differences between two groups were analyzed using the two-tailed Student's *t* test. Threshold of significance was taken as $p < 0.05$.

RESULTS

ATM Is Activated by Oxidative Stress in Vascular Endothelial Cells—To investigate the involvement of ATM in mediating oxidative stress in the vasculature, we first examined the acti-

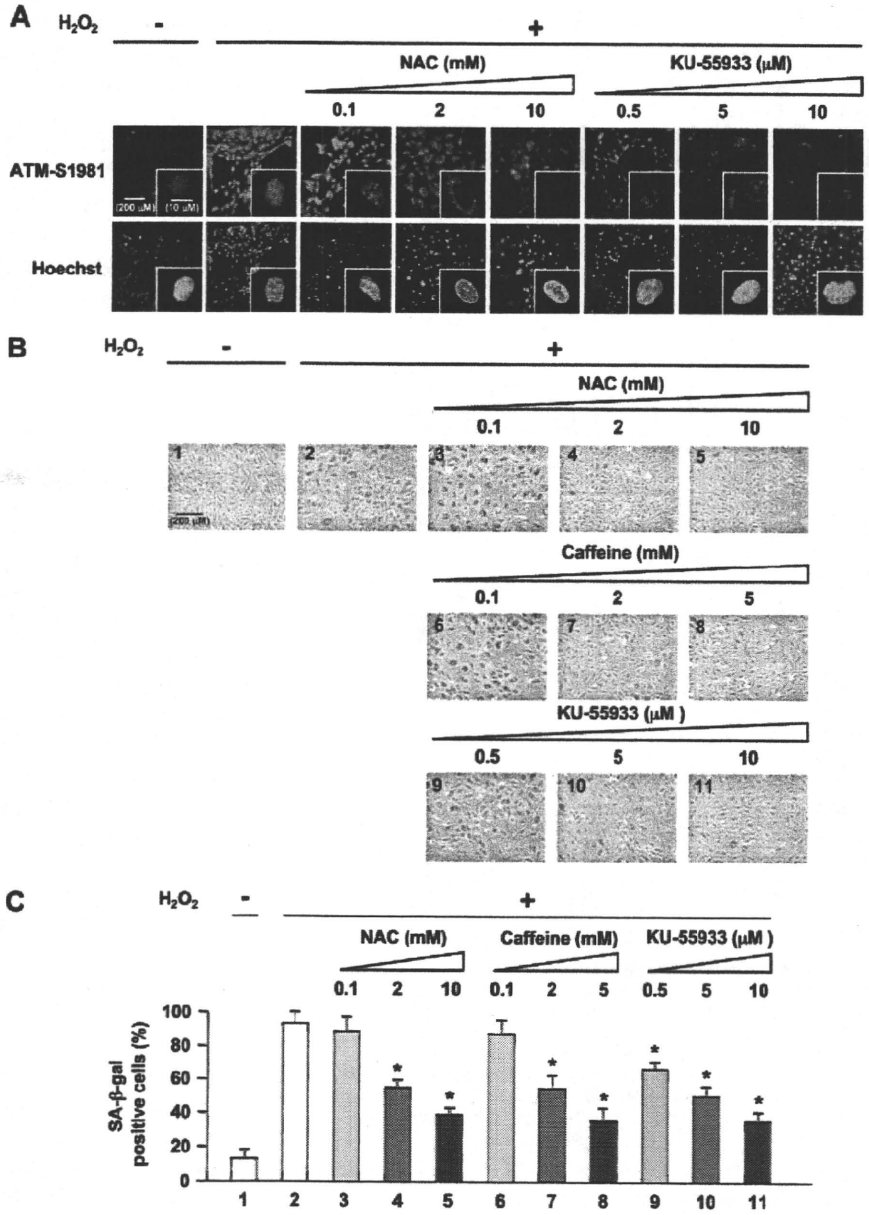

FIGURE 3. **Oxidative stress-induced endothelial cell senescence involves activation of ATM kinase.** *A*, immunofluorescence analysis of the effects of antioxidant (NAC) and ATM inhibitor (KU-55933) on phosphorylated ATM. Cells were treated with NAC or KU-55933 followed by 100 μM H_2O_2 for 1 h and then immunostained for phosphorylated ATM-S1981. Hoechst 33258 was used as nuclear stain (*blue*). Original magnification, ×200 and ×630. Higher magnification of the representative cells in *A* is shown in supplemental Fig. 2. *Scale bar*, 200 μm and 10 μm, respectively. NAC or KU-55933 greatly reduced phosphorylated ATM nuclear fluorescence and foci formation. *B*, effects of NAC, caffeine, or KU-55933 on premature senescent phenotype induced by H_2O_2 as shown by SA-β-gal staining. *C*, quantification of percentage of SA-β-gal-positive cells in *B*. Values are mean ± S.E. (*error bars*) ($n = 3$). *, $p < 0.05$ *versus* cells incubated with H_2O_2. Original magnification, ×100. *Scale bar*, 200 μm. Pretreatment with NAC, caffeine, or KU-55933 resulted in significant reduction of senescent (SA-β-gal-positive) cells compared with those exposed to H_2O_2 alone.

(Fig. 1*D* and supplemental Fig. 1*A*) (18). Total ATM, in contrast, remained diffusely localized throughout the nucleus, and foci formation was not observed in H_2O_2-treated HUVECs (Fig. 1*F* and supplemental Fig. 1*C*). Activated (phosphorylated) ATM localized to foci, which suggests that it might be recruited to sites of DNA damage caused by oxidative stress (17, 18). However, the authors note that the antibody used (ATM-S1981) is known to also recognize a nonspecific protein, which makes conclusions based on experiments using this antibody inconclusive. We further investigated expression of 53BP1 and γ-H2AX as markers of DSB formation in response to H_2O_2 by immunostaining. In the H_2O_2-treated cells, both 53BP1 and γ-H2AX formed nuclear foci (supplemental Fig. 3), which further supports that ATM is activated in response to DSB formation induced by H_2O_2.

Activation of the ATM-dependent DNA Damage Signaling Pathway Contributes to Endothelial Cell Senescence—To better confirm actions of activation of ATM by oxidative stress in endothelial cells, effects of inhibitors of oxidative stress and of ATM were tested. HUVECs were pretreated with NAC, an antioxidant and glutathione precursor that alters the redox state of cells (19), to assess whether ATM phosphorylation was caused by H_2O_2-induced redox imbalance. Western blot analysis showed that pretreatment of endothelial cells with NAC blocked the stimulatory effects of H_2O_2 on the expression of ATM-S1981, Akt-S473, p53-S15 (*lanes 3–5* in Fig. 2*A*) and p21 (*lanes 3–5* in Fig. 2*D*). These results suggest a direct role of H_2O_2 in ATM phosphorylation and activation of involved genes. We further employed two inhibitors, caffeine and KU-55933, to inhibit ATM kinase activity to examine whether Akt and p53 activation as well as p21 up-regulation induced by H_2O_2 is dependent on the ATM protein kinase. Caffeine is known to disrupt ATM-dependent responses likely through direct inhibition of ATM kinase activity (20), and KU-55933 is a specific and potent inhibitor of ATM kinase (21). Both inhibitors inhibited H_2O_2-induced ATM (Ser^{1981}), Akt (Ser^{473}), and p53 (Ser^{15}) phosphorylation (*lanes 3–5* in Fig. 2, *B* and *C*), in addition to p21 induction (*lanes 6–8* and *lanes 11–13* in Fig. 2*D*). Thus, ATM kinase played a major role in transducing H_2O_2-induced DNA damage signaling in HUVECs. Because an Akt/p53/p21-dependent pathway has been reported in endothelial cells (6), ATM thus likely regulates the cellular response to oxidative stress via phosphorylation of Akt and p53 then induction of p21 in sequence. Furthermore, NAC or KU-55933 also

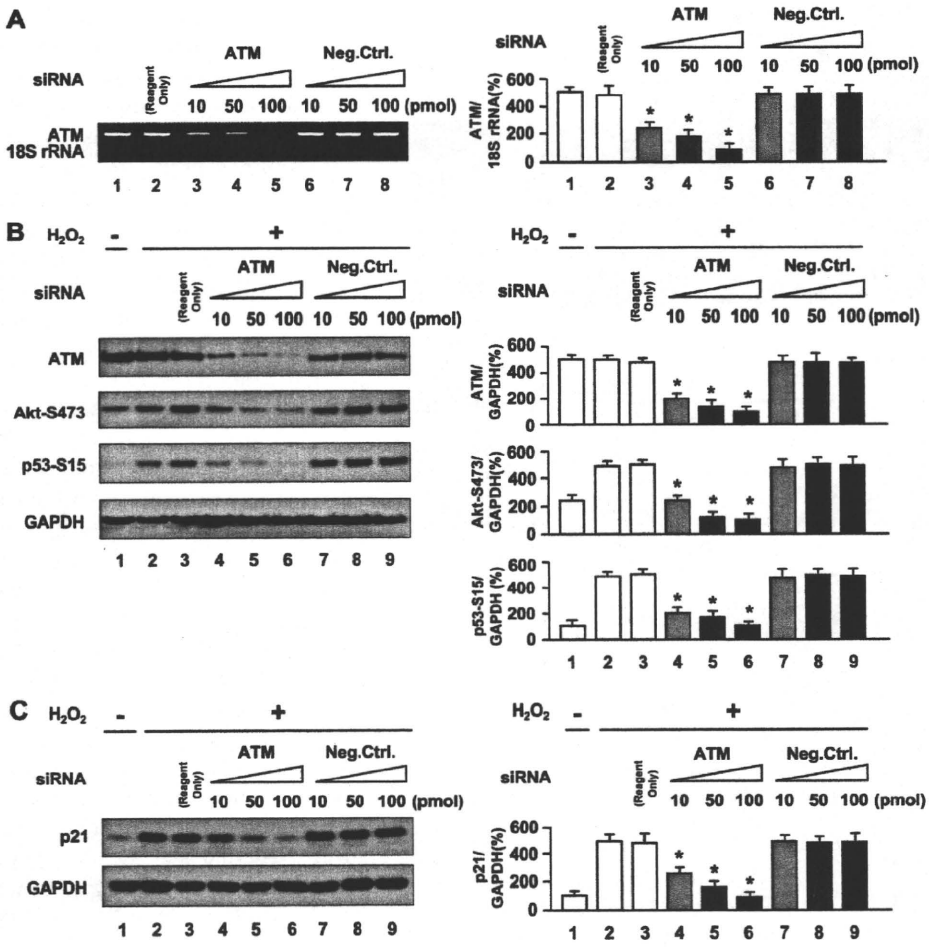

FIGURE 4. **Knockdown of ATM by ATM siRNA inhibits oxidative stress-induced activation of Akt and p53 and induction of p21 expression.** *A*, effect of siRNA against ATM on expression of ATM as analyzed by RT-PCR. *B* and *C*, Western blot analysis of the effects of siRNA against ATM on expression of total ATM, Akt phosphorylation (Ser^{473}), p53 phosphorylation (Ser^{15}), and p21 induction. Cells were transfected with siRNA against ATM for 72 h followed by incubation with 100 μM H_2O_2 for 30 min in *B* or 3 h in *C*. GAPDH was used as loading control. Values are mean ± S.E. (*error bars*) ($n = 3$). *, $p < 0.05$ *versus* cells transfected with the same concentration of negative control siRNA. Representative blots are shown in the *left panels* whereas corresponding quantitations are shown in the *right panels*. *Reagent Only*, cells transfected with Lipofectamine 2000 alone.

greatly reduced phosphorylated ATM nuclear fluorescence and foci formation (Fig. 3*A*). Collectively, H_2O_2 induced DNA damage and stimulated autophosphorylation of ATM in addition to formation of discrete nuclear foci together with subsequent induction of phosphorylation of Akt, p53, and up-regulation of p21 expression in an ATM-dependent manner.

Because the DNA damage response pathway triggers senescence (22) and because p53 and p21 were described to be major players in the induction of senescence (23, 24), we next addressed the functional effects of activation of the ATM/Akt/p53/p21 pathway on endothelial cells, namely in the form of induction of senescence which is a consequence of endothelial dysfunction. We induced premature endothelial senescence by addition of H_2O_2 to 100 μM as shown by SA-β-gal assay, a recognized surrogate index of senescent cells (25). We found that percentage of HUVECs positive for SA-β-gal was markedly increased in cells treated with H_2O_2, compared with cells incubated without H_2O_2 treatment (*panel 2* in Fig. 3*B* and *lane 2* in Fig. 3*C*). Furthermore, pretreatment with NAC, caffeine, or KU-55933 resulted in significant reduction of senescent (SA-β-gal-positive) cells compared with those exposed to H_2O_2 alone (Fig. 3, *B* and *C*). Thus, activation of ATM by H_2O_2 promotes endothelial cell senescence and contributes to vascular pathogenesis.

Abrogation of ATM Blocks Effects of Oxidative Stress on Endothelial Cells—We further examined the requirement of ATM expression in H_2O_2-induced premature senescence by abrogating ATM in cells using RNA interference. Knockdown of ATM in HUVECs by siRNA reduced ATM mRNA and protein levels (Fig. 4, *A* and *B*). Cells transfected with ATM siRNA showed reduced ATM expression with inhibition of Akt and p53 phosphorylation (*lanes 4–6* in Fig. 4*B*) in addition to down-regulation of p21 expression (*lanes 4–6* in Fig. 4*C*). As expected, ATM nuclear fluorescence was also markedly decreased in cells with ATM knocked down (Fig. 5*A*). Furthermore, knockdown of ATM by siRNA suppressed increase in SA-β-gal-positive cells induced by H_2O_2 (*panels 5* and *6* in Fig. 5*B* and *lanes 5* and *6* in Fig. 5*C*), which were comparable with the changes seen when HUVECs were treated with antioxidant or ATM inhibitor. Moreover, down-regulation of Akt, p53, or p21 by siRNA also suppressed an increase in SA-β-gal-positive cells induced by H_2O_2 (supplemental Figs. 4 and 5). Thus, RNA interference experiments further confirmed that ATM and its downstream molecules, Akt, p53, and p21, mediate actions of oxidative stress on endothelial cells to induce senescence.

Abrogation of Senescent Phenotype in Aorta of ATM Knock-out Mice—To test whether ATM mediates vascular endothelial cell senescence *in vivo*, we administered STZ to ATM knock-out mice and wild-type littermates to induce hyperglycemia-induced endothelial dysfunction because vascular endothelial cell senescence has been previously documented to be induced in STZ-diabetic mice (26). Western blot analysis for ATM protein levels in the thoracic aortas of heterozygous knock-out mice showed marked reductions to levels almost comparable with those of homozygote knock-out mice in contrast to robust levels as seen in wild-type mice (Fig. 6*B* and supplemental Fig. 7*A*) although the mechanisms of reduced protein levels in heterozygous knock-out mice are unclear. STZ-treated mice showed an elevation in blood glucose levels compared with STZ-untreated mice (*lanes 2, 4,* and *6* in Fig. 6*C*). SA-β-

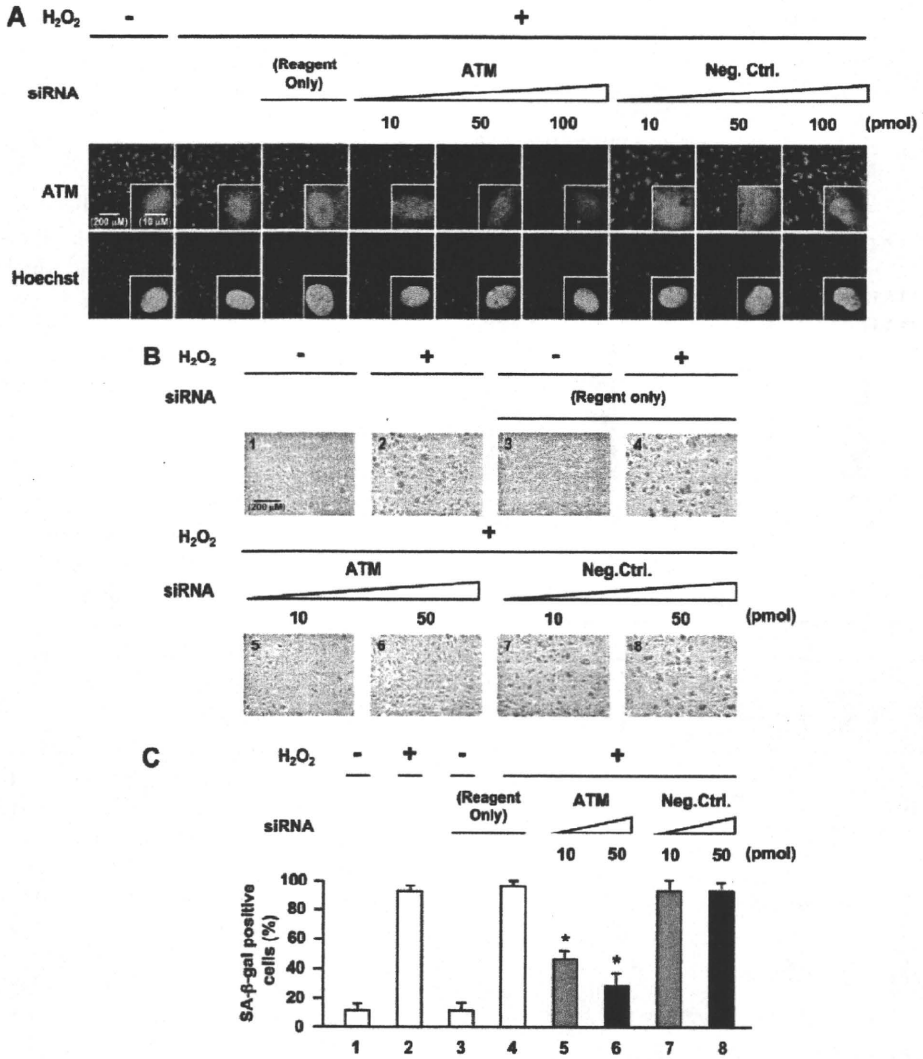

FIGURE 5. **Effects of abrogation of ATM expression by siRNA against ATM in oxidative stress-induced endothelial senescence.** *A*, immunofluorescence analysis of the effect of siRNA against ATM on total ATM. Transfected cells were immunostained for total ATM. Hoechst 33258 was used as nuclear stain (*blue*). Original magnification, ×200 and ×630. *Scale bar*, 200 μm and 10 μm, respectively. ATM nuclear fluorescence was greatly decreased in ATM knock-down cells. *B*, staining of SA-β-gal activity in ATM knock-down cells. *C*, quantification of percentage of SA-β-gal-positive cells in ATM knock-down cells. Values are mean ± S.E. (*error bars*) ($n = 3$). *, $p < 0.05$ *versus* cells transfected with the same concentration of negative control siRNA (*lane 7* or *lane 8*, respectively) ($n = 3$ each). Original magnification, ×100. *Scale bar*, 200 μm. *Reagent Only*, cells transfected with Lipofectamine 2000 alone. Knockdown of ATM by siRNA suppressed the increase in SA-β-gal-positive cells induced by H_2O_2.

gal activity was observed in the thoracic aortas of STZ-diabetic wild-type mice but not in STZ-diabetic ATM knock-out mice (Fig. 6, *D* and *E*). Cross-sections of thoracic aortas stained with SA-β-gal showed that positive areas were mostly localized to the luminal surface (Fig. 6*F*) which also stained positive for von Willebrand factor, indicating localization to vascular endothelial cells and not the extracellular matrix compared with normal rabbit IgG antibody (Fig. 6*G* and supplemental Fig. 6*A*). p21 and p16 are cyclin-dependent kinase inhibitor genes that are used as senescence markers. SA-β-gal-positive areas of cross-sections of thoracic aortas stained positive for p21 and p16 (Fig. 6*H* and 6*I*) but not for normal mouse IgG antibody used as a negative control (supplemental Fig. 6*B*). These results indicate that ATM is important for the induction of endothelial cell senescence in aortas of STZ-diabetic mice, which is consistent with *in vitro* cellular experiments.

DISCUSSION

Oxidative stress caused by reactive oxygen species plays an important causal role in senescence and age-related vascular diseases, including atherosclerosis and diabetic vasculopathy (7, 27, 28). Despite the wealth of knowledge on the effects and actions of oxidative stress on endothelial cells, characterization of involved regulatory pathways allowing for targeted molecular intervention with therapeutic intent had remained elusive.

We showed that ATM is involved in oxidative stress-induced endothelial dysfunction and premature senescencethroughanAkt/p53/p21-dependent pathway. Cellular experiments using HUVECs showed that the ATM/Akt/p53/p21 pathway was involved in oxidative stress-induced cellular senescence *in vitro*. Experiments using antioxidant and specific ATM inhibitory compounds or siRNA against ATM inhibited oxidative stress-induced cellular senescence thus confirming involvement of ATM and its dependent pathway. Furthermore, ATM induced endothelial cellular senescence *in vivo* in the aorta of diabetic wild-type mice but not in ATM knock-out mice. STZ-diabetic $ATM^{+/-}$ mice exhibit reduction in SA-β-gal-positive cells to levels almost comparable with those seen in STZ-diabetic $ATM^{-/-}$ mice. Reduction of ATM protein expression in heterozygote knock-out mice may account for the difference seen in endothelial senescence between wild-type and heterozygous knock-out mice. Collectively, the findings presented here indicate the importance of ATM in the induction of endothelial cell senescence induced by oxidative stress and abrogation of ATM resulting in a dysregulated response to pathophysiological stress in cardiovascular endothelial cells.

We further showed that ATM lies upstream from the Akt/p53/p21 pathway and that oxidative stress as sensed through ATM possibly in response to oxidative DNA damage is the initiating "trigger" and plays an instructive role in activation of this signaling pathway. Previous studies also demonstrated that ATM is a major upstream activator of Akt through control of

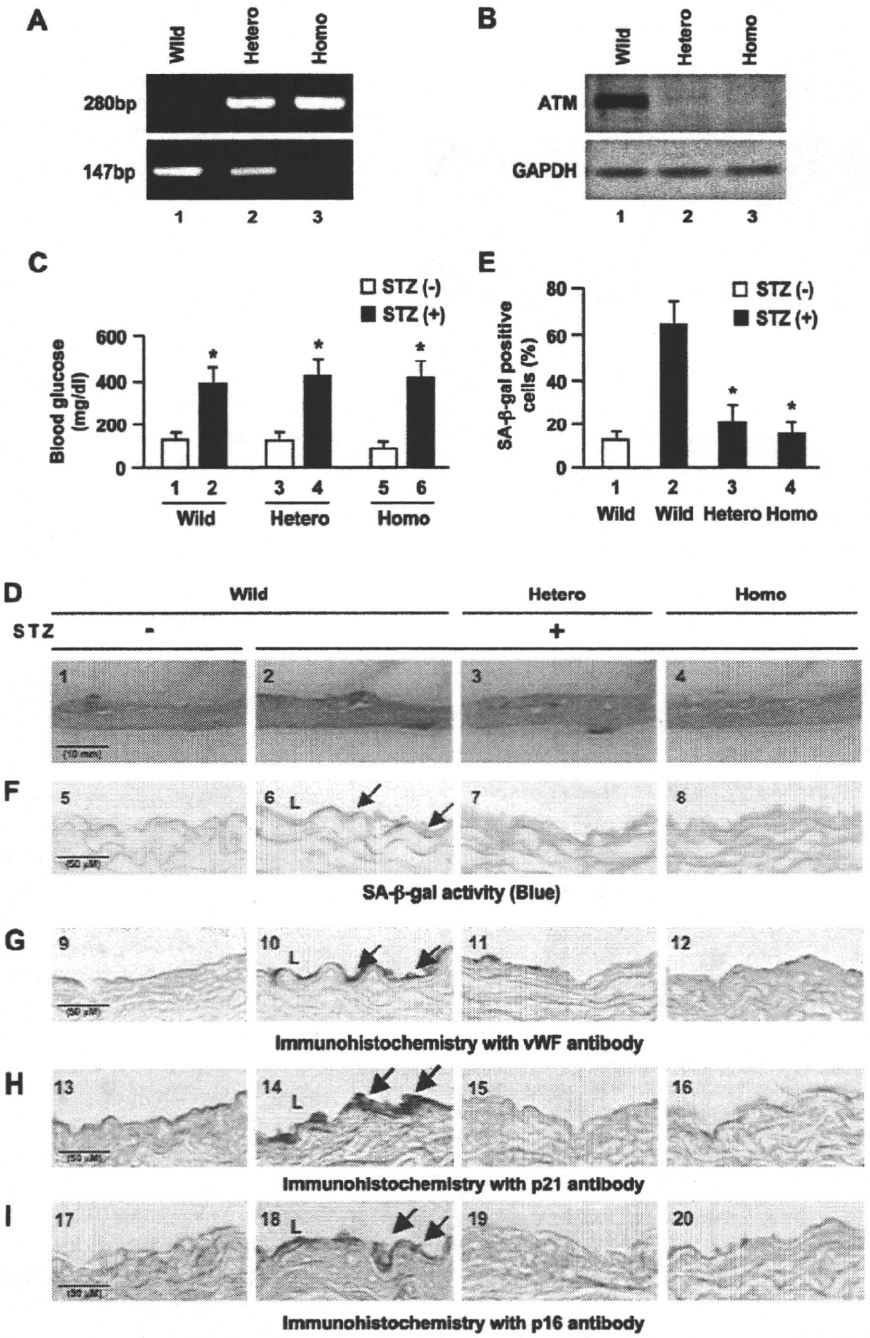

FIGURE 6. **Senescent endothelial cells in aortas of STZ-diabetic ATM knock-out mice.** Six respective $ATM^{+/+}$ (*Wild*), $ATM^{+/-}$ (*Hetero*), and $ATM^{-/-}$ (*Homo*) mice were used. *A*, genotyping analysis for ATM mice. *B*, Western blot analysis of ATM expression in the thoracic aortas. *C*, blood glucose levels measured before and after treatment with STZ. Values are mean ± S.E. (*error bars*). *, $p < 0.05$ *versus* STZ (−) mice (*lane 1*, *lane 3*, or *lane 5*, respectively). *D*, SA-β-gal activity (*blue*) in the thoracic aortas from mice at 10 days after treatment with STZ. *E*, quantitation of percentage of SA-β-gal-positive cells in the STZ-treated thoracic aortic samples. Values are mean ± S.E. *, $p < 0.05$ *versus* STZ (+) mice. *F*, sections of SA-β-gal stained thoracic aortas. *Arrows* indicate SA-β-gal-positive cells mostly localized to the luminal surface in the cross-section of the thoracic aortas. *G*, immunohistochemistry for von Willebrand factor, an endothelial cell marker, in the thoracic aortas (*brown*). *Arrows* indicate positive staining in the endothelium. *H* and *I*, immunohistochemical staining of p21 and p16 (*brown*). *Scale bar*, 50 μm and 10 mm, respectively.

cells stimulated by oxidative stress, we demonstrated for the first time to our knowledge that ATM regulates endothelial senescence through activation of Akt. Further, the pathway downstream of Akt through p53 and p21 has been well studied as a central pathophysiological signaling pathway in endothelial cells, especially in response to insulin (6, 7). However, whether the Akt/p53/p21 pathway is also activated by oxidative stress has not been clear. Our results thus indicate that this pathway is activated by oxidative damage and most importantly, regulated by ATM. γ-H2AX and 53BP1 foci formation was induced by oxidative stress, thus further providing supportive evidence that the oxidative stress-induced ATM-Akt/p53/p21 pathway is activated by DNA DSBs (supplemental Fig. 3).

Although the DNA damage response has been pursued mainly in oncogenesis and cancer-related fields and recently in regulation of senescence (1–3), as ATM has been shown to be activated by oxidative stress in hematopoietic cells (8), it is not beyond reason and in fact quite reasonable that ATM and the DNA damage response are involved in the vasculature as a response to oxidative stress albeit unexpected and unappreciated. Previous studies by ourselves initially suggested that the DNA damage response is activated in cardiovascular pathogenesis through the action of poly(ADP-ribose)polymerase-1 (PARP-1) (30), but identification and characterization of the actions of the central signaling molecule, ATM, in cardiovascular regulation provides further compelling evidence for the importance of this pathway in regulation of the vasculature and its diseases.

Our findings might explain in part the underlying mechanisms of the congenital disease condition of A-T in which the ATM gene is mutated. One of the hallmark characteristic phenotypes of A-T is vascular dysplasia and dysfunction, which pronounces as telangiectasia. Pathologically, vascular degeneration as characterized by loss of elastic fibers and proliferation of smooth muscle cells is seen. Patients that sur-

Ser^{473} phosphorylation in response to insulin or ionizing radiation, which results in radiosensitivity or resistance to insulin in cell lines derived from A-T patients and ATM knock-out mice (15) or in muscle cells (29). However, in vascular endothelial

vive to later years are also known to be prone to ischemic heart disease (31). Although the precise underlying mechanism for the latter is unknown, in general, progression of coronary artery disease involves accelerated atherosclerosis in which oxidative stress of the endothelium and related cells plays a major contributory role. Response to oxidative stress in the vasculature may be disrupted in A-T patients. Dysregulation of endothelial cell function might lead to pathophysiological states such as vascular dysfunction in developmental states and accelerated atherosclerosis in adults. Better understanding the cellular response to oxidative stress with a focus on ATM is expected to shed further light on the pathogenesis of A-T and to clarify alternative pathological pathways that are activated in response to oxidative stress when deficient for ATM as well as to provide new insight into the molecular mechanisms underlying age-related cardiovascular pathologies such as atherosclerosis in which ATM might pose a new therapeutic target for vascular pathologies involving oxidative stress.

In conclusion, we show that oxidative stress can induce cellular senescence in HUVECs as shown by staining for SA-β-gal, which was associated with an ATM-dependent Akt/p53/p21 signaling pathway. Our findings might in part explain underlying mechanisms of the pathogenesis of the disease ataxia telangiectasia in which vascular dysplasia and dysfunction are seen, as well as suggesting that ATM may be a new therapeutic target for cardiovascular pathologies.

REFERENCES

1. Bartkova, J., Rezaei, N., Liontos, M., Karakaidos, P., Kletsas, D., Issaeva, N., Vassiliou, L. V., Kolettas, E., Niforou, K., Zoumpourlis, V. C., Takaoka, M., Nakagawa, H., Tort, F., Fugger, K., Johansson, F., Sehested, M., Andersen, C. L., Dyrskjot, L., Ørntoft, T., Lukas, J., Kittas, C., Helleday, T., Halazonetis, T. D., Bartek, J., and Gorgoulis, V. G. (2006) *Nature* **444,** 633–637
2. Bartkova, J., Horejsí, Z., Koed, K., Krämer, A., Tort, F., Zieger, K., Guldberg, P., Sehested, M., Nesland, J. M., Lukas, C., Ørntoft, T., Lukas, J., and Bartek, J. (2005) *Nature* **434,** 864–870
3. Gorgoulis, V. G., Vassiliou, L. V., Karakaidos, P., Zacharatos, P., Kotsinas, A., Liloglou, T., Venere, M., Ditullio, R. A., Jr., Kastrinakis, N. G., Levy, B., Kletsas, D., Yoneta, A., Herlyn, M., Kittas, C., and Halazonetis, T. D. (2005) *Nature* **434,** 907–913
4. Zeiher, A. M., Drexler, H., Saurbier, B., and Just, H. (1993) *J. Clin. Invest.* **92,** 652–662
5. Breitschopf, K., Zeiher, A. M., and Dimmeler, S. (2001) *FEBS Lett.* **493,** 21–25
6. Miyauchi, H., Minamino, T., Tateno, K., Kunieda, T., Toko, H., and Komuro, I. (2004) *EMBO J.* **23,** 212–220
7. Minamino, T., and Komuro, I. (2007) *Circ. Res.* **100,** 15–26
8. Ito, K., Hirao, A., Arai, F., Matsuoka, S., Takubo, K., Hamaguchi, I., Nomiyama, K., Hosokawa, K., Sakurada, K., Nakagata, N., Ikeda, Y., Mak, T. W., and Suda, T. (2004) *Nature* **431,** 997–1002
9. Barzilai, A., Rotman, G., and Shiloh, Y. (2002) *DNA Repair* **1,** 3–25
10. Shiloh, Y. (2003) *Nat. Rev. Cancer* **3,** 155–168
11. Ota, H., Eto, M., Kano, M. R., Ogawa, S., Iijima, K., Akishita, M., and Ouchi, Y. (2008) *Arterioscler. Thromb. Vasc. Biol.* **28,** 1634–1639
12. Bakkenist, C. J., and Kastan, M. B. (2003) *Nature* **421,** 499–506
13. Kozlov, S. V., Graham, M. E., Peng, C., Chen, P., Robinson, P. J., and Lavin, M. F. (2006) *EMBO J.* **25,** 3504–3514
14. Dupré, A., Boyer-Chatenet, L., and Gautier, J. (2006) *Nat. Struct. Mol. Biol.* **13,** 451–457
15. Viniegra, J. G., Martínez, N., Modirassari, P., Losa, J. H., Parada Cobo, C., Lobo, V. J., Luquero, C. I., Alvarez-Vallina, L., Ramón y Cajal, S., Rojas, J. M., and Sánchez-Prieto, R. (2005) *J. Biol. Chem.* **280,** 4029–4036
16. Lavin, M. F. (2008) *Nat. Rev. Mol. Cell Biol.* **9,** 759–769
17. Bencokova, Z., Kaufmann, M. R., Pires, I. M., Lecane, P. S., Giaccia, A. J., and Hammond, E. M. (2009) *Mol. Cell. Biol.* **29,** 526–537
18. Rappold, I., Iwabuchi, K., Date, T., and Chen, J. (2001) *J. Cell Biol.* **153,** 613–620
19. Zafarullah, M., Li, W. Q., Sylvester, J., and Ahmad, M. (2003) *Cell. Mol. Life Sci.* **60,** 6–20
20. Zhou, B. B., Chaturvedi, P., Spring, K., Scott, S. P., Johanson, R. A., Mishra, R., Mattern, M. R., Winkler, J. D., and Khanna, K. K. (2000) *J. Biol. Chem.* **275,** 10342–10348
21. Hickson, I., Zhao, Y., Richardson, C. J., Green, S. J., Martin, N. M., Orr, A. I., Reaper, P. M., Jackson, S. P., Curtin, N. J., and Smith, G. C. (2004) *Cancer Res.* **64,** 9152–9159
22. von Zglinicki, T., Saretzki, G., Ladhoff, J., d'Adda di Fagagna, F., and Jackson, S. P. (2005) *Mech. Ageing Dev.* **126,** 111–117
23. Brown, J. P., Wei, W., and Sedivy, J. M. (1997) *Science* **277,** 831–834
24. Kang, J. Y., Kim, J. J., Jang, S. Y., and Bae, Y. S. (2009) *Mol. Cells* **28,** 489–494
25. Dimri, G. P., Lee, X., Basile, G., Acosta, M., Scott, G., Roskelley, C., Medrano, E. E., Linskens, M., Rubelj, I., Pereira-Smith, O., Peacocke, M., and Campisi, J. (1995) *Proc. Natl. Acad. Sci. U.S.A.* **92,** 9363–9367
26. Yokoi, T., Fukuo, K., Yasuda, O., Hotta, M., Miyazaki, J., Takemura, Y., Kawamoto, H., Ichijo, H., and Ogihara, T. (2006) *Diabetes* **55,** 1660–1665
27. Finkel, T., and Holbrook, N. J. (2000) *Nature* **408,** 239–247
28. Davies, K. J. (2000) *IUBMB Life* **50,** 279–289
29. Halaby, M. J., Hibma, J. C., He, J., and Yang, D. Q. (2008) *Cell. Signal.* **20,** 1555–1563
30. Suzuki, T., Nishi, T., Nagino, T., Sasaki, K., Aizawa, K., Kada, N., Sawaki, D., Munemasa, Y., Matsumura, T., Muto, S., Sata, M., Miyagawa, K., Horikoshi, M., and Nagai, R. (2007) *J. Biol. Chem.* **282,** 9895–9901
31. Swift, M., and Chase, C. (1983) *Lancet* **1,** 1049–1050.

Leukemia Research 34 (2010) e21–e24

Contents lists available at ScienceDirect

Leukemia Research

journal homepage: www.elsevier.com/locate/leukres

Letter to the Editor

Erdheim–Chester disease: Multisystem involvement and management with interferon-α

Erdheim–Chester disease (ECD) is a rare, non-Langerhans form of histiocytosis of unknown origin, with involvement of skeletal system and multiple organs [1]. Recently, interferon-α (IFN-α) has been reported as a valuable therapy for ECD [2,3]. We report another case of ECD treated with IFN-α and discuss the therapeutic efficacy.

A 47-year-old Japanese male presented to our hospital with 2-year history of multiple xanthogranulomas (xanthelasmas) on the both eyelids and face, periorbital congestion and exophthalmos. Thoracoabdominal CT scanning and magnetic resonance imaging (MRI) disclosed soft-tissue infiltration in the renal pelvis and uterus, bilateral hydronephrosis and periaortic fibrosis ("coated aorta" appearance) (Fig. 1A–D). A periorbital skin biopsy demonstrated diffuse infiltration with CD68+/S100−/CD1a− foamy histiocytes and Touton giant cells (Fig. 2), leading to the diagnosis of ECD. The long bone radiographs and bone scintigraphy showed a symmetric medullary sclerosis of the femur and tibia, which is a characteristic radiological feature of ECD (Fig. 1E and F). Furthermore, brain MRI revealed the absence of hyperintensity of the posterior pituitary lobe on T1-weighted images, without sellar mass lesions or stalk thickening, and hormonal examinations were compatible with diabetes insipidus (Fig. 1G). Initial complete blood counts showed a white blood cell count of 9.0×10^9/l with a normal differential count, a hemoglobin level of 9.5 g/dl, and a platelet count of 541×10^9/l.

The renal function gradually worsened, and required the insertion of ureteral stent on the right kidney. Renal scintigraphy showed a remarkable decrease in left kidney uptake, suggesting severe renal impairment due to chronic renal obstruction and xanthomatous invasion (Fig. 1H). Renovascular hypertension was also observed. Since the periaortic infiltration also extended to the aortic arch and pericardial region with the presence of pericardial effusion, the treatment with IFN-α was initiated (3×10^6 units, subcutaneously 3 times per week). Treatment was generally well tolerated, except for fever following injections. IFN-α treatment improved xanthelasmas after 1 month and attenuated the substantial progression of pericardial effusion. Renal function has been kept managable with ureteral stenting and diuretics. Thirteen months later, IFN-α was transiently discontinued due to progression of anemia caused by renal impairment, which recovered within 2 months. IFN-α was reintroduced, maintained at the dose of 3×10^6 units twice per week for 8 months, and then tapered to once per week. The patient's condition remained generally stable after 32 months of follow up with IFN-α therapy, except for the slow progression of the renal impairment.

Since the initial description in 1930, about 250 cases of ECD were reported in the literature. The most frequent clinical features of ECD are bone pain, exophthalmos and diabetes insipidus. Renal and retroperitoneal involvement frequently occurs in about 30% (17/59) of ECD patients in isolation or as a component of disseminated disease [1]. The "hairy kidney" appearance on CT scans is highly suggestive of the diagnosis [4]. This affectation is usually asymptomatic, but can present with dysuria, abdominal pain, enlarged palpable kidneys and ureteric obstruction, leading to hydroneprosis and acute or chronic renal failure. The prognosis of ECD is generally worse than that of Langerhans cell histiocytosis, and pulmonary involvement and cardiac failure are regarded as the most common causes of death [1,2,5]. Severe renal failure could also result in the emergent complication or the fatal outcome in some cases [6–8].

There is no standard treatment for ECD owing to its rarity, while several options including steroids, various cytotoxic agents and hematopoietic stem cell transplantation have been reported with variable effects [1,9]. IFN-α has been recently shown to be a promising treatment for ECD [2,3,10]. In the Braiteh's report, marked improvement was noted in three patients, with regression of retro-orbital disease within 1 month and gradual and durable improvement of bone lesions, pain and diabetes insipidus over the following month [2]. Otherwise, the efficacy of IFN-α varies among the sites of disease involvement, and especially cardiovascular and central nervous system involvement, and mesenteric lesions may resist to IFN-α treatment [3,11]. As for renal disease, IFN-α seems to effective for ureteral obstruction, allowing withdrawal of ureteral stents, in two patients in the Haroche's report describing eight patients' responses [3]. In our case, xanthelasmas responded well to IFN-α, and IFN-α treatment appears to be effective in preventing progression of cardiovascular and renal involvements. Thus, early therapeutic intervention by IFN-α may be important for stabilization of ECD, although the occurrence of life-threatening events such as myocardial infarction and acute renal failure should also be kept in mind during the IFN-α treatment, as in our case. Whereas IFN-α might be a valuable first-line therapy for ECD at the present time, the establishment of further effective therapeutic modality is warranted, considering the slow progression of renal impairment in our case. Failure of IFN therapy might lead to more aggressive or

0145-2126/$ – see front matter
doi:10.1016/j.leukres.2009.07.026

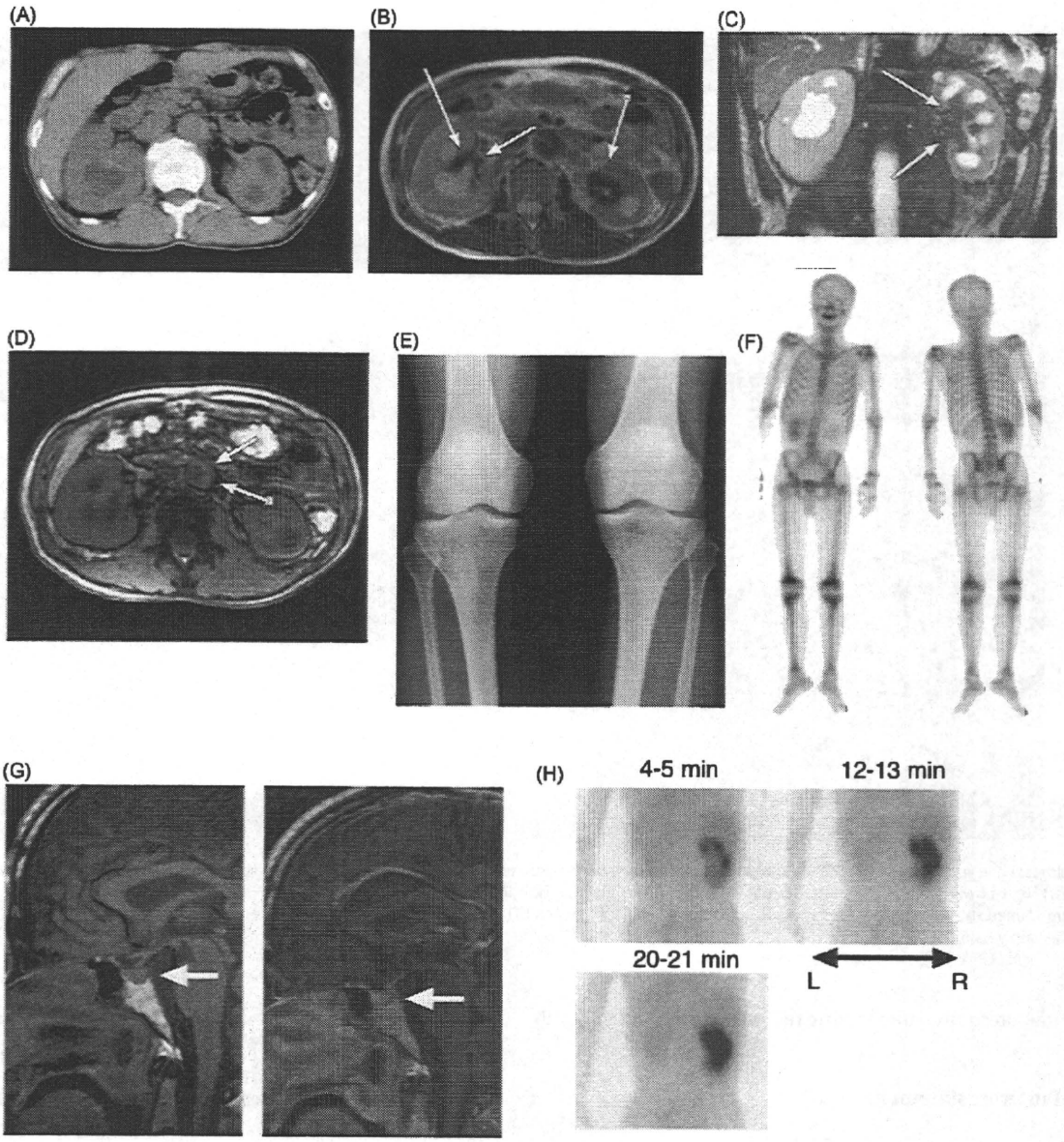

Fig. 1. Radiological findings. Abdominal CT (A) and MRI (B) show soft-tissue infiltration in the both renal pelvis (arrows) and associated hydronephrosis. Left renal parenchyma is thinned, suggesting chronic renal impairment. (C) A coronal reformatted enhanced image showing bilateral pelvocaliectasis (arrows). (D) Abdominal MRI scan with periaortic infiltration ("coated aorta") (arrows). Bone radiograph (E) and scintigraphy (F) showing a symmetric medullary sclerosis of the femur and tibia. (G) Brain MRI shows the absence of hyperintensity of the posterior pituitary lobe (arrows) on T1-weighted image, which is also evident after contrast enhancement (right). (H) Renal scintigraphy demonstrates the abrogation of left kidney uptake.

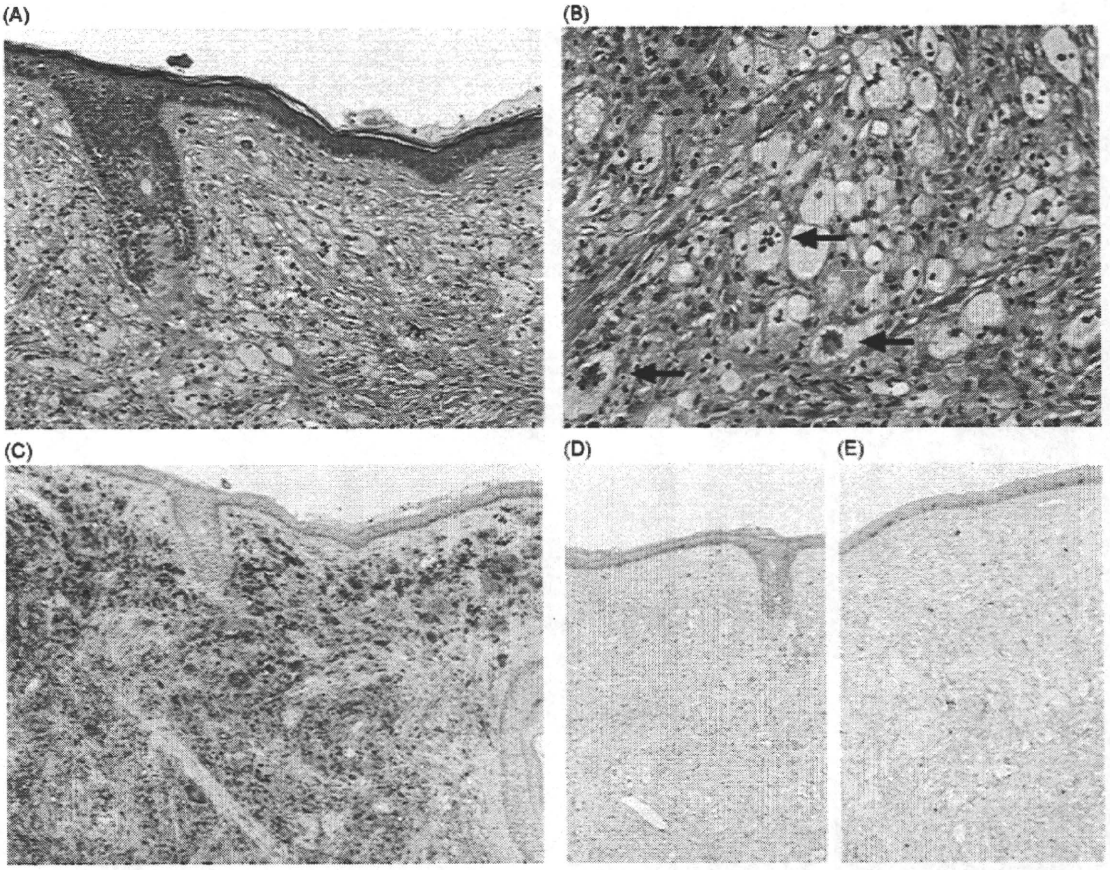

Fig. 2. Histological and immunohistochemial findings of the skin biopsy. (A) Hematoxylin–Eosin (H–E) stains, 100×. Skin biopsy shows dense infiltration of large foamy histiocytes. (B) High-power view of H–E staining. Arrows show Touton giant cells. Immunohistochemistry for CD68 (C), S100 (D) and CD1a (E) (brown), 100×. The foamy histiocytes are stained strongly positive for CD68 (C), but negative for S100 (D) and CD1a (E). (For interpretation of the references to color in this figure legend, the reader is referred to the web version of the article.)

experimental alternative therapeutic regimens including imatinib [12].

Conflict of interest statement

All authors declare that there are no competing financial interests regarding this article.

Acknowledgement

This manuscript was not supported with any financial or other relationships.

References

[1] Veyssier-Belot C, Cacoub P, Caparros-Lefebvre D, Wechsler J, Brun B, Remy M, et al. Erdheim–Chester disease. Clinical and radiologic characteristics of 59 cases. Medicine (Baltimore) 1996;75(3):157–69.
[2] Braiteh F, Boxrud C, Esmaeli B, Kurzrock R. Successful treatment of Erdheim–Chester disease, a non-Langerhans-cell histiocytosis, with interferon-alpha. Blood 2005;106(9):2992–4.
[3] Haroche J, Amoura Z, Trad SG, Wechsler B, Cluzel P, Grenier PA, et al. Variability in the efficacy of interferon-alpha in Erdheim–Chester disease by patient and site of involvement: results in eight patients. Arthritis Rheum 2006;54(10):3330–6.
[4] Dion E, Graef C, Haroche J, Renard-Penna R, Cluzel P, Wechsler B, et al. Imaging of thoracoabdominal involvement in Erdheim–Chester disease. AJR Am J Roentgenol 2004;183(5):1253–60.
[5] Haroche J, Amoura Z, Dion E, Wechsler B, Costedoat-Chalumeau N, Cacoub P, et al. Cardiovascular involvement, an overlooked feature of Erdheim–Chester disease: report of 6 new cases and a literature review. Medicine (Baltimore) 2004;83(6):371–92.
[6] Rush WL, Andriko JA, Galateau-Salle F, Brambilla E, Brambilla C, Ziany-bey I, et al. Pulmonary pathology of Erdheim–Chester disease. Mod Pathol 2000;13(7):747–54.
[7] O'Rourke R, Wong DC, Fleming S, Walker D. Erdheim–Chester disease: a rare cause of acute renal failure. Australas Radiol 2007;51(Spec No.):B48–51.
[8] Verdalles U, Goicoechea M, Garcia de Vinuesa S, Mosse A, Luno J. Erdheim–Chester disease: a rare cause of renal failure. Nephrol Dial Transplant 2007;22(6):1776–7.
[9] Gaspar N, Boudou P, Haroche J, Wechsler B, Van Den Neste E, Hoang-Xuan K, et al. High-dose chemotherapy followed by autologous hematopoietic stem cell transplantation for adult histiocytic disorders with central nervous system involvement. Haematologica 2006;91(8):1121–5.
[10] Loddenkemper K, Hoyer B, Loddenkemper C, Hermann KG, Rogalla P, Forster G, et al. A case of Erdheim–Chester disease initially mistaken for Ormond's disease. Nat Clin Pract Rheumatol 2008;4(1):50–5.
[11] Perlat A, Decaux O, Sebillot M, Grosbois B, Desfourneaux V, Meadeb J. Erdheim–Chester disease with predominant mesenteric localization: lack of efficacy of interferon alpha. Joint Bone Spine 2009;76(3):315–7.
[12] Haroche J, Amoura Z, Charlotte F, Salvatierra J, Wechsler B, Graux C, et al. Imatinib mesylate for platelet-derived growth factor receptor-beta-positive Erdheim–Chester histiocytosis. Blood 2008;111(11):5413–5.

Hiroshi I. Suzuki[a], Noriko Hosoya[a,b], Kiyoshi Miyagawa[a], Satoshi Ota[c], Hiroko Nakashima[d], Noriko Makita[e], Mineo Kurokawa[a,*]
[a] *Department of Hematology and Oncology, Graduate School of Medicine, University of Tokyo, 7-3-1 Hongo, Bunkyo-ku, Tokyo 113-8655, Japan*
[b] *Department of Cell Therapy and Transplantation Medicine, Graduate School of Medicine, University of Tokyo, Tokyo, Japan*

[c] Department of Pathology, Graduate School of Medicine, University of Tokyo, Tokyo, Japan
[d] Department of Dermatology, Graduate School of Medicine, University of Tokyo, Tokyo, Japan
[e] Department of Endocrinology and Nephrology, Graduate School of Medicine, University of Tokyo, Tokyo, Japan

* Corresponding author. Tel.: +81 3 5800 9092; fax: +81 3 5840 8667.
E-mail address: kurokawa-tky@umin.ac.jp (M. Kurokawa)

28 May 2009
Available online 12 August 2009